Thickness dependence of electron transport in amorphous selenium for use in direct conversion flat panel X-ray detectors

A Thesis

Submitted to College of Graduate Studies and Research

in Partial Fulfillment of the Requirements for the Degree of Masters of Science in the

Department of Electrical and Computer Engineering

University of Saskatchewan

By

Derek Mortensen

Saskatoon, Saskatchewan

Permission to use

In submitting this thesis for partial fulfillment of the requirements of a Masters of Science degree from the University of Saskatchewan I agree that the Libraries of this University may make it freely available for inspection. Further I agree that permission to copy this thesis in whole or part for scholarly purposes may be granted by the professor or professors who supervised this work, or in their absence, the Head of the Department of the Dean of the College where my work was completed. Copying in whole or part of this thesis for financial gain shall not be allowed without written approval from myself and the University of Saskatchewan.

Requests for permission to copy or use any material in this thesis in whole or part should be addressed to:

Heads of the Department of Electrical and Computer Engineering
Engineering Building, 57 Campus Drive
University of Saskatchewan
Saskatoon, SK, S7N5A9
Canada

Abstract

Amorphous Selenium (a-Se) was first commercialized for use as a photoconductor in xerography during the middle of the twentieth century. Since then the hole transport properties of a-Se have been studied extensively, however the study of electron transport remains relatively limited. Flat panel digital X-ray detectors using a-Se as a photoconductor have been developed and are being used in mammographic screening. The charge transport properties of the photoconductor layer will in part determine the performance of the flat panel detector. X-ray absorption causes electron-hole pair generation in the bulk of the photoconductor, requiring both electrons and holes to drift across the sample and be collected. If these carriers are lost in the many localized trapping states as they cross the sample, they will not contribute to the image signal resulting in unnecessary radiation exposure to the patient.

Eleven a-Se samples were deposited at the University of Saskatchewan varying in thickness from 13 μm to 501 μm. Pure a-Se was chosen to ensure uniformity across the thickness of the samples, that is, to ensure the composition of the film did not change across the thickness. Time of flight transient photoconductivity experiments (TOF) and interrupted field time of flight (IFTOF) measurements were performed to measure the electron drift mobility and lifetime respectively. The product of electron drift mobility μ and lifetime τ, hence the carrier range ($\mu\tau$) at a given applied electric field. The electron range is an important parameter as this places limits on the practical thickness of the photoconducting layer in a detector. This study also includes an investigation into the effect of the definition of transit time on the calculated drift mobility and analysis of the dispersive transport properties of a-Se.

It was observed that as sample thickness (L) increased, electron drift mobility (μ) decreased. In addition electron lifetime (τ) decreased dramatically in samples thinner than 50 μm. Electron range ($\mu\tau$) was 2.26×10^{-6}cm^2/V in the 147μm sample and 5.46×10^{-8} cm^2/V in the 13 μm sample, a difference of almost two orders of magnitude. The comparison of the half current method and inflection point methods to calculate the transit time of the same TOF curve, shows that the calculated mobility can vary by as much as 24%. This illustrates clearly that it is important to use the same point on the TOF curve to define the transit time. Charge packet dispersion (spread) in the time domain in pure a-Se samples was proportional to L^m where L is the photoconductor thickness and $m \sim 1.3$, measured at both 1 V/μm and 4 V/μm.

Acknowledgements

I extend my sincerest gratitude to my family, friends, and supervisor for their support, patience, and encouragement throughout this project. This thesis would not have been possible without financial support from the University of Saskatchewan, NSERC, and the Anrad Corporation.

1 Table of Contents

List of Figures

List of Tables

1 X-Ray Imaging

1.1 Introduction

Since their discovery in the late 19th century X-rays have become a valuable diagnostic tool. The ability to quickly examine a patient internally without invasive surgery brought about significant changes in the practice of medicine. For many decades these radiographic systems were improved but at the beginning of the 21st century many of these tools are still using a film based emulsion to capture the X-ray image. These emulsions are often encased in an X-ray cassette, and covered in a phosphor screen to convert the incident X-rays to visible light. This X-ray cassette is only good for one exposure and must be developed using the traditional chemical process. Replacing this film-based method with a digital X-ray detector provides many advantages.

In order to replace the X-ray cassette and its analogue emulsion with a digital system, at some point in the imaging chain the incident X-rays must be converted to an electrical signal. This can either be done indirectly using a phosphor screen in a system similar to the analogue method, which converts the X-rays to visible light that can then be captured by either a CCD imaging system or by a an a-Si:H based active matrix array in which each pixel has a photodiode. Indirect conversion has advantages, however the thickness of the phosphor required to absorb and convert the incident X-rays will inherently limit the spatial resolution of an indirect detector. The resolution can be improved by using a phosphor with a columnar structure to guide the light to the pixels.

Direct conversion X-ray detectors capture and separate the electron-hole pairs (EHP) created by the incident X-ray photons directly with no intermediate conversion step. This approach has several advantages when compared to indirect conversion; first the spatial resolution is not limited by the phosphor in front of the

read out array, as the generated charge is drifted perpendicular to the detector surface by an applied bias. Secondly, if the photoconductor is suitably chosen, all X-ray generated electrons and holes can be collected without any loss to carrier trapping or recombination.

1.2 History of X-Ray Detectors

1.2.1 Principles of Radiography

X-ray effects were first observed in the late 19th century and the first direct observation and documentation is generally credited to Wilhelm Rontgen. Figure 1.1 illustrates the limited resolution and contrast of early X-ray images.

Figure 1.1 The oldest known X-ray image, captured by Rontgen showing his wife's hand and wedding ring (after Kevles et al. [1]).

Soon after being discovered and used to capture the first image, X-rays were being used to aid diagnosis; a clear sign of their potential in the medical field. It became clear very soon after their discovery that X-rays damage living tissue and since then, there has been a constant struggle to gather as much information as possible from an X-ray exposure while minimizing the patient X-ray dose. There have been many

different types of X-ray detectors developed, which can be classified based on how the radiation interacts with the detector.

The principle of an X-ray detector is to form an image from by measuring the amount of radiation passing through a subject at different points over the image area. It is not practical to build a lens to bend X-ray photons so the sensor area must be slightly larger than the desired image area. As the X-rays pass through the subject some of the radiation will be absorbed by the body and not reach the detector. This variation in attenuation is what produces contrast in the image. The amount of attenuation depends on the incident photon energy, the subject density, and the subject thickness. A simplified X-ray imaging chain is shown in Figure 1.2, the chain includes an X-ray source (further detailed in Figure 1.3), a collimator stage to convert the radiation from the X-ray source to a parallel beam, the patient, and finally an X-ray detector to capture the image.

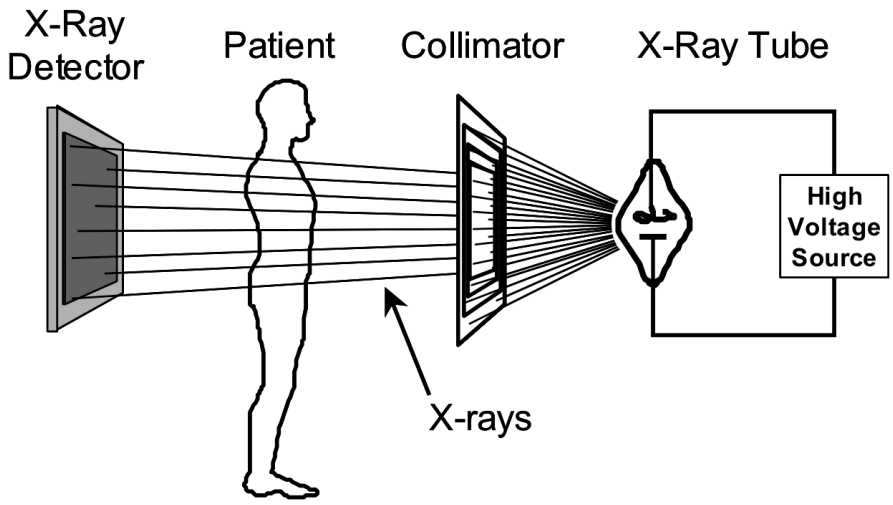

Figure 1.2 Basic diagram of an X-ray imaging system. The system consists of an X-ray source, a collimator to ensure the photos are travelling perpendicular to the detector; the patient is placed between the collimator and the X-Ray detector. The detector records the spatial intensity pattern of X-rays passing through the patient, which can then be viewed as an image (after Fogal [2]).

Patient dose is defined as the amount of ionizing radiation absorbed during exposure. Patient dose is an important consideration in the field of medical imaging as high doses of radiation cause health problems it is important to minimize the dose applied to the patient while still capturing a useful image.

Ionizing detectors are the focus of study in this work. An ionizing detector works when the incident X-rays modify some property of the detector, either physical or chemical, that generates free charge inside the detector. The amount of generated charge will be proportional to the amount of incident radiation. This charge can then be separated, collected and counted in order to determine exposure at a particular location in the detector.

A *radio-luminescent* (*or an X-ray luminescent*) *detector* uses a scintillator, which absorbs the incident radiation and emits a small quantity of light some time later. This light emission can occur almost immediately after exposure (within 10^{-6} to 10^{-8} seconds) or in the case of some materials require some additional input such as heat. The storage properties of radio luminescent detectors mean that they can be irradiated for long periods of time and heated at a later date to measure the amount of radiation received over the testing period which will be proportional to the light emitted upon heating. Thermo-luminescent dosimeters (TLDs), are small X-ray luminescent detectors, which can be worn by workers to monitor radiation dose, operate on this principle.

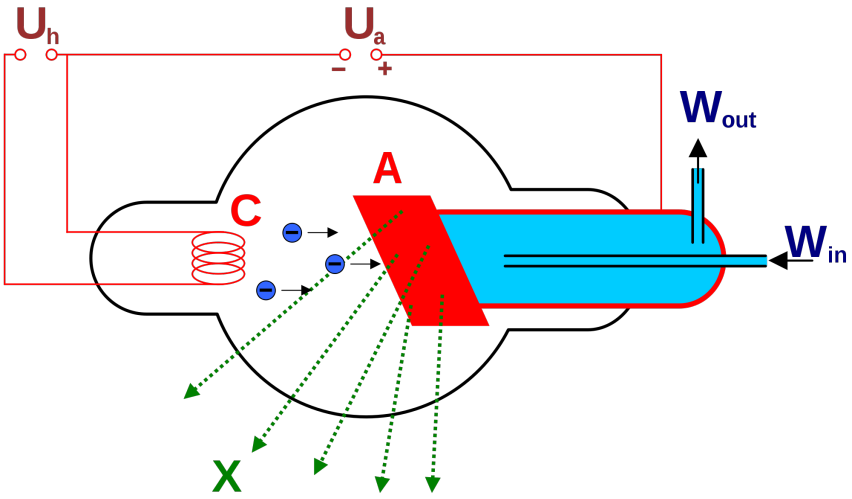

Figure 1.3 A water-cooled Coolidge X-Ray tube diagram. A high voltage between the cathode and anode (~100kV) accelerates electrons which strike a rotating tungsten target, this collision between high energy electrons and the atoms of the target emits a broad spectrum of X-rays which are then channeled through the collimator composed of perforated thin lead sheets to create a beam of X-rays which is nearly perpendicular to the detector (pubic domain image).

Different measurement types will place different constraints on the image detector design. For example a typical chest X-ray involves imaging a large area with large features [3]. Capturing an image of a broken bone inside the chest cavity requires a much different design than detecting microcalcifications as small as 10^{-4} m in diameter in a mammographic exam [4].

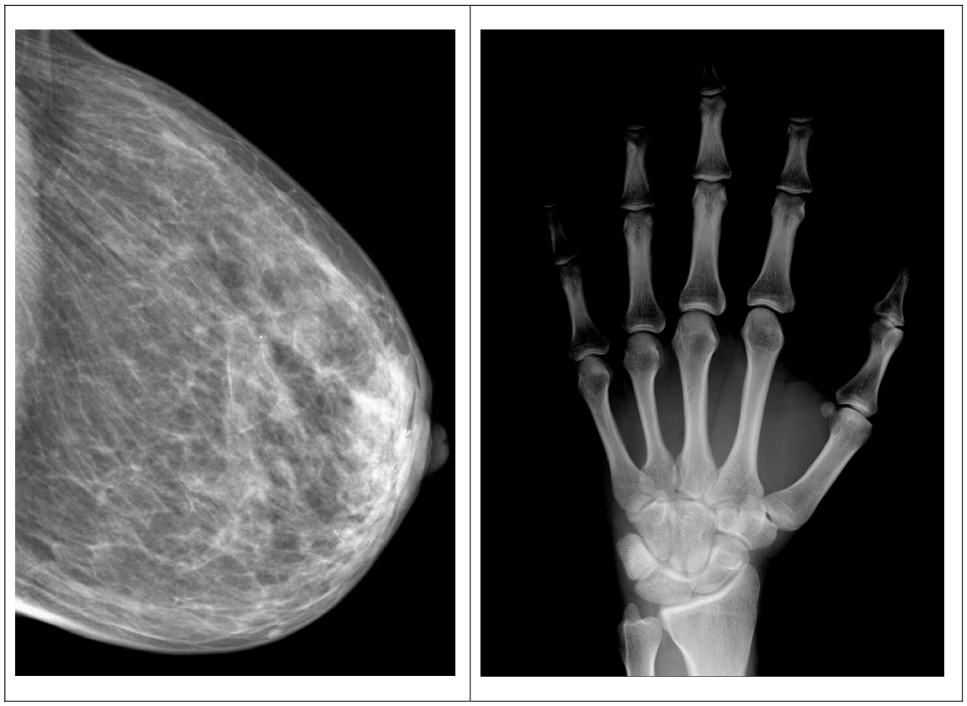

Figure 1.4 Two X-ray images captured by Direct Conversion Flat Panel detectors (after Kasap and Rowlands [5]).

Figure 1.4 shows a bone X-ray image of a wrist and hand shows that the denser bone tissue absorbed more of the incident X-ray radiation and thus shows up lighter in the negative image, while the soft tissue surrounding the bone absorbed very little radiation and thus is almost transparent. This type of X-ray requires a large area as well as a large dynamic range to see detail in both bone and soft tissue in the same image. This is opposed to the mammographic image shown on the left; in this case the entire image is composed of tissue so the dynamic range of the detector is not as important as the absolute resolution and contrast. In the case of mammographic scans, physicians are often looking for very small lesions or microcalcifications with

diameter on the order of 10^{-4}m that are surrounded by tissue of very similar density.

1.2.2 Materials used in X-ray Photodetectors

Though technology for general-purpose digital imaging has progressed rapidly over the last two decades, the transition to digital X-ray image capture has lagged behind and traditional analogue processes to capture X-ray images remain in wide use. Though digital X-ray image capture has many advantages including: faster image acquisition, potential of lower radiation dose, easy image archiving, and speed of image sharing if a the opinion of a second physician is required, the requirement of large image area image sensors is outside the capability of crystalline based sensors used in general purpose imaging where lenses can be used to focus the incident light.

1.2.2.1 Analogue X-ray image capture

Traditional X-ray imaging techniques use a combination of a phosphor film and a large sheet of photographic film that is sensitive to photons in the visible light range. Figure 1.5 expands on the general diagram of Figure 1.2 for the case film based image capture. A phosphor sheet absorbs the incident X-ray radiation after it has passed through the patient and emits photons proportionally in the visible range. This visible light is absorbed by the photographic film, which can then be developed to form a negative image.

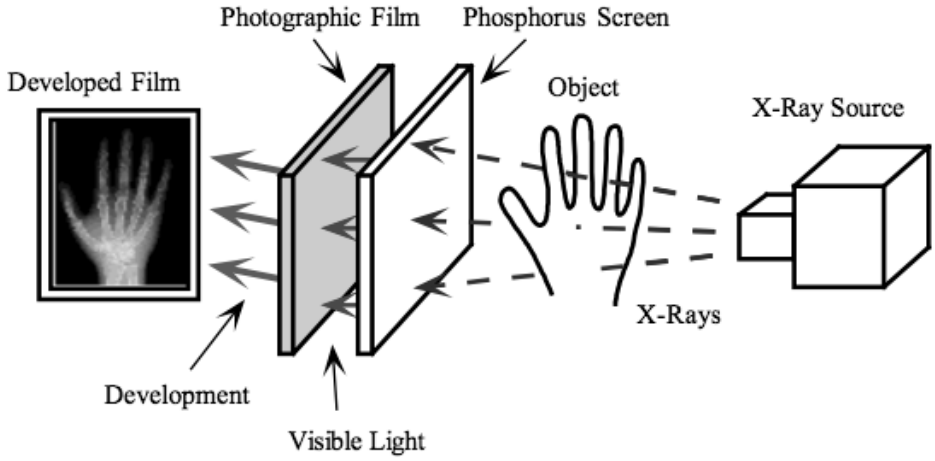

Figure 1.5 An overview of the traditional film based method of capturing X-ray images (after Allen [6]).

Though this method has been fine tuned over the last century since the discovery of X-ray imaging and can provide image quality sufficient to diagnose many bone related ailments, it has many disadvantages in comparison to a digital system [3]. A film based system requires the sheet of photographic film to be developed after exposure, a process that takes at least several minutes. This limits the ability of a technician to identify problems with the image and retake it immediately if necessary. Once developed, a sheet of photographic film requires a backlight to view and to transmit the image either the film needs to be scanned which is time consuming, or the original negative must be shipped. This difficulty in archiving and sharing the image can lead to repeat X-ray images being taken by different physicians, resulting in more radiation exposure for the patient [7].

In the past several decades there has been an effort to replace this film based system with digital detectors [8]. Capturing an X-ray image digitally eliminates many of these problems, though the design of such a device has presented many challenges because of the size and resolution of detector required.

1.2.2.2 Classification of digital X-ray Detectors

There are two main categories of digital X-ray image detectors [9]: indirect and direct. Indirect X-ray detectors generate an electrical signal from the incident X-ray photos by first passing the X-rays through a phosphor screen and then collecting the

visible light photons that are emitted by the screen [5]. This is similar to the film based technique but replaces the photographic film with a photodetector array. The indirect conversion method is resolution limited by the phosphor screen stage, as this conversion from X-ray to visible light photons will always cause some lateral spread in the emitted photons. As mentioned above, the resolution can be improved by using columnar phosphors to guide the emitted light towards the pixels of the photodetector array.

Direct conversion detectors eliminate the phosphor screen and absorb the X-ray photons directly before converting them to an electrical signal to form an image. Direct conversion detectors using amorphous selenium (a-Se) as the absorption and photoconducting medium are the subject of this study. A typical direct conversion X-ray detector uses a large active matrix array panel consisting of rows and columns of pixels. This panel is coated with a layer of a-Se sandwiched between two metal electrodes [3]. The incident X-ray photons are absorbed in the bulk of the a-Se creating free electrons and holes, which are drifted apart by an applied electric field, collected at the pixels, and the amount of charge on each pixel is be read out to form an image. The amount of charge on each pixel will be proportional to the intensity of the incident X-ray beam at that location on the detector after it has passed through the patient.

Direct conversion detectors will have a higher inherent resolution as they eliminate any lateral spread caused by the phosphor screen before the photons reach the detector [3], this is important in mammography because of the high resolution required to detect small lesions. By carefully selecting the thickness, composition, and applied bias of the a-Se layer, absorption efficiency can be optimized to minimize the patient dose by using as much of the X-ray beam as possible.

Digitizing the X-ray images allows images to be viewed very quickly after capture, easy image archival and retrieval, the ability to quickly transmit an image to another

physician if a second opinion is required, and allows the design of higher resolution detectors that minimize the radiation dose to the patient.

1.2.3 Structure of a Direct Conversion X-Ray detector

To form an X-ray image the incident beam of photons must be sampled and recorded in both the spatial and intensity domains. In direct conversion flat panel detectors this is accomplished by coating a large area active matrix array (AMA) of pixels with an amorphous photoconductor such as a-Se sandwiched between two electrodes that apply an electric field across the photoconductor [4]. The incident X-ray photons are absorbed in the bulk of the photoconductor creating free electron-hole pairs (EHP), which are then separated and drifted to the charge collecting pixels by the applied electric field.

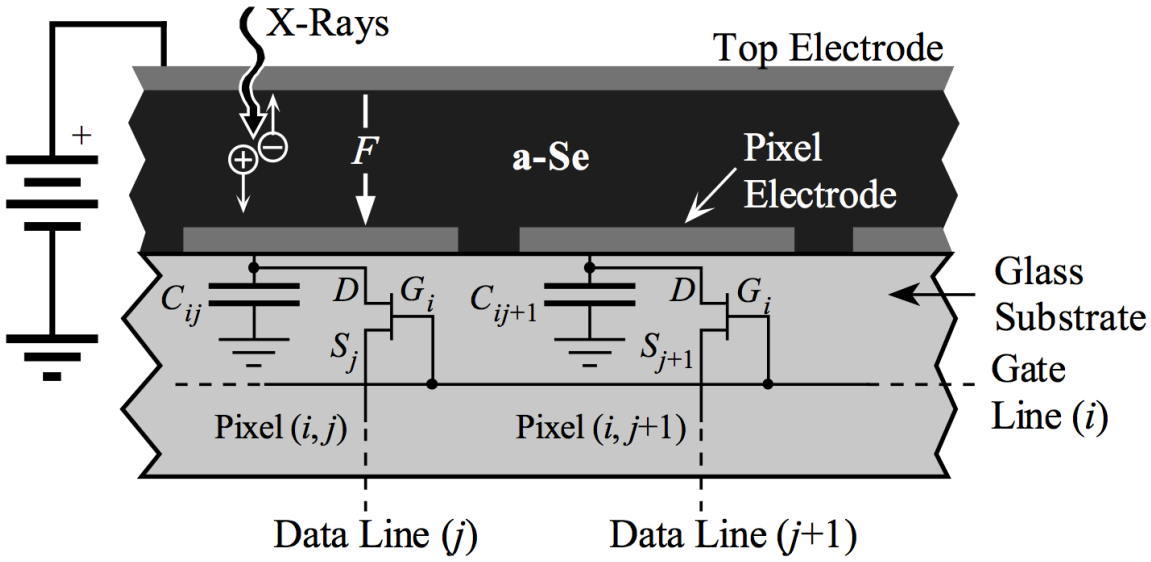

Figure 1.6 A cross sectional view of two pixels in a direct conversion flat panel detector using a-Se as the photo conducting material (after Allen [6]).

As shown in Figure 1.6 the charge generated in the bulk of the photoconductor is drifted to the pixel electrodes and stored in the pixel capacitor. After the generated charge carriers reach the pixel electrodes, the amount of stored charge can be read out and will be proportional to the amount of X-ray radiation absorbed in the area of each pixel on the detector. By activating each *i* line, the amount of charge on each

pixel Δq_{ij} is read out on the j line of the active matrix array. This signal is then digitized and sent to a computer in the form of an image as shown in Figure 1.7

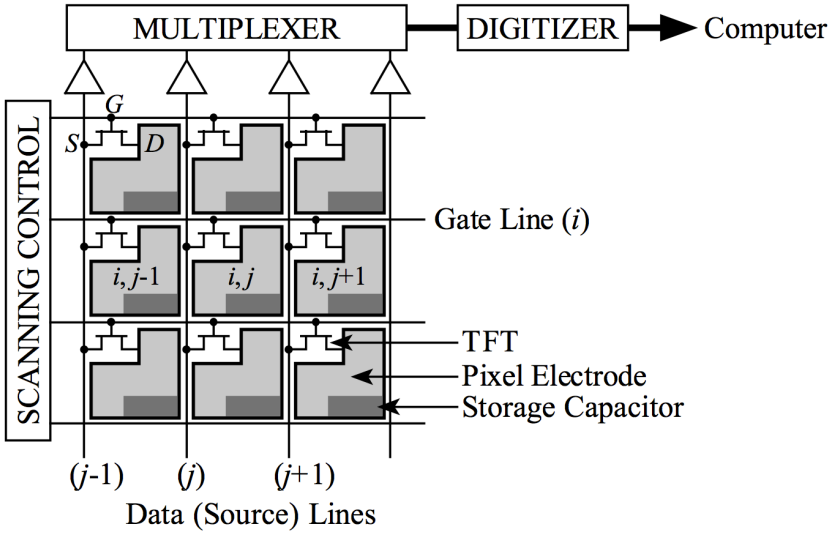

Figure 1.7 A view of nine pixels on a thin film transistor (TFT) active matrix array (AMA) for use in a direct conversion X-ray image detector (after Allen [6]).

As mentioned above, a digital X-ray image is formed by sampling the incident X-ray beam in both the spatial and intensity domains after it has been modulated while passing through the patient. In flat panel direct conversion X-ray image detectors, the sampling is accomplished with the pixel structure of an AMA, the spatial resolution of the detector will normally be limited by the pixel size, allowing detection of smaller calcifications in mammographic scans, which require pixels on the order of 50 μm [8].

1.2.4 Modes of Detector Operation

It is assumed above that a single incident X-ray photon generates some charge Q in the bulk of the photoconductor at time t = 0 [8], this generated charge will then be drifted to the pixel electrode, collected, and read out. As the charge is drifting to the collecting electrode it will generate a current in the external circuit $i(t)$, the time integral of this generated current from t = 0 when the charge was created to $t = t_c$ must equal the amount of generated charge Q.

$$Q = \int_{t=0}^{t_c} i(t)dt \qquad 1.1$$

The modes of detector operation can be broadly classified as pulse mode and current mode. When a detector is operating in pulse mode, each individual absorption event is distinguishable from the next; the arrival of the X-ray radiation is randomly distributed, governed by Poisson statistics. When operating in pulse mode the detector can record both the total charge absorbed in the detector and the energy of each individual radiation quanta that is absorbed by the photoconducting layer.

As the pulse rate increases it will no longer be possible to distinguish each individual pulse from the next, and in this case, the detector is said to be operating in current mode. The output from the detector is a time dependent average of the current created by the moving charge in the detector. If we assume a fixed response time, the current produced between $t - t_r$ and t is given by

$$I(t) = \frac{1}{t_r} \times \int_{t-t_r}^{t} i(t')\, dt \qquad 1.2$$

The output from the detector is the product of the average event rate over the sampling time T and the charge produced by each event [9].

$$I_o = rQ = r\frac{E}{W_{\pm}}q \qquad 1.3$$

where

r is the event rate

Q is charge generated by each event

E is average energy deposited for each event

$W_{\pm}$ is average energy required to produce an EHP

$q = 1.6 \text{ x } 10^{-19}$ C is charge of electron

In practical applications, any detector that is required to measure the energy of individual incident photons must operate in pulse mode. An example is the positron emission spectroscopy (PES) detectors used in brain imaging. The vast majority of medical X-ray image detectors do not require the individual quanta energy to be recorded and operate in current mode.

1.2.5 Ideal X-Ray Photoconductor

This work involves the use of amorphous Selenium (a-Se) as the photoconducting layer coated on the AMA array, however before delving into the properties of a-Se it is useful to define an ideal photoconducting material to provide a benchmark for the development of higher quality materials.

1) High X-ray absorption; any radiation that has passed through the patient and is not absorbed by the detector is wasted and causes unnecessary radiation exposure to the patient.
2) Small electron hole pair (EHP) creation energy ($W_{\pm}$); this will ensure that as much charge as possible is generated from the incident photons.
3) In order to maximize the signal to noise ratio the dark current of the detector should be zero. On real world detectors this can be accomplished by using large bandgap photodetectors, but this is in direct opposition to 2 as they will have a higher value of $W_{\pm}$, the use of non injecting contacts helps achieve this.
4) There should be no recombination of the generated electron hole pairs as they are drifted by the applied electric field to the collecting electrodes.
5) Carrier Schubweg defined as the average distance a carrier will travel before being trapped should be larger than the thickness of the photoconductor to ensure that the generated charge reaches the electrodes before being trapped.

6) To ensure the charge has reached the pixel electrodes before they are read out the carrier transit time must be shorter than the access time of the pixels.
7) These properties should not change due to repeated X-ray exposure over time.
8) As large area detectors are required the photoconductor should be easily coated over large areas without damaging the AMA components due to high temperatures.

Though these are the properties of an ideal X-ray photoconducting material (list modified from [2]), which does not exist in real world applications, a-Se has been shown to meet many of these requirements [9].

1.3 Amorphous selenium X-Ray Detectors

1.3.1 X-Ray Absorption

The purpose of the a-Se photoconducting layer is to convert the incident X-ray photons into an electrical signal. The photons are absorbed within the bulk of the material due to the photoelectric effect; creating free electron hole pairs. This free charge is then drifted across the sample by an applied bias, collected at the electrodes, and read out to form an image. The first step of this process is the absorption of incident X-rays; any radiation that passes through the detector without being absorbed results in unnecessary radiation exposure to the patient as it has not contributed to the image. X-ray absorption is characterized by the attenuation coefficient α, which is a physical property of the material. The fraction of the incident photons that will be attenuated within a thickness L is given by

$$A_Q(E) = [1 - \exp(-\alpha L)] \qquad 1.4$$

where α = α (E,Z,d) is the linear attenuation coefficient of the material which depends on the energy of the incident X-ray photons (E), the atomic number of the

material (Z) and the density of the material (d). The absorption depth δ is defined as $1/\alpha$ and at that depth 63% of the incident radiation will have been attenuated.

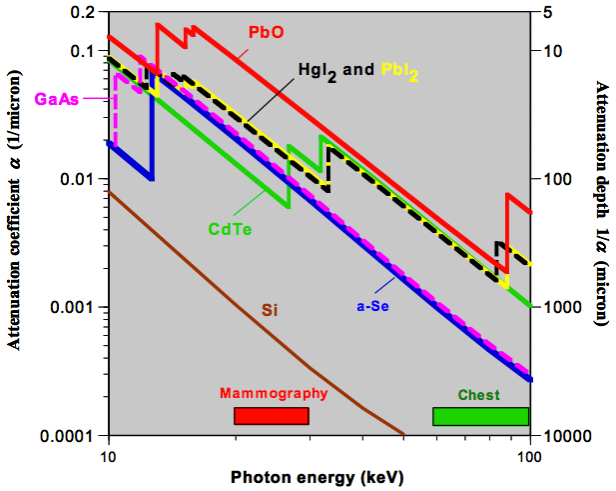

Figure 1.8 The linear attenuation coefficient α and absorption depth (1/ α) of a-Se and other amorphous semiconductors of interest as a function of the incident photon energy in the X-ray spectrum (After Kasap et al. [5])

The sharp edges shown in Figure 1.8 are related to the emission of electrons from inner shells to the conduction band. By identifying these K, and L atomic shells edges different materials can be compared for their use in chest and mammographic digital X-ray image detectors. The absorption coefficient will typically increase with increasing Z as $\alpha \propto Z^m$ where $m \approx$ 3-5 which is why lead (Z = 82) is commonly used as an X-ray shield.

The desire to absorb as many incident photons as possible suggests the use of a thick layer of a-Se such as $L = 5\delta$ where ~98% of the incident radiation will be attenuated. However there are other factors in the detector design that limit the thickness of the photoconducting layer. First, as the thickness of the layer increases so must the applied voltage bias, which is typically greater than 10 V/μm, so a layer of 500 μm would require an applied bias exceeding 5000 V. Secondly, it is difficult and expensive to fabricate very thick photoconductor layers that are free of inhomogeneities and defects [2]. Thirdly, as the layer increases in the thickness, the free charges must travel much further to reach the electrodes; this slows the

detector response time and increases the number of charge carriers that will be trapped within the photoconductor, and never collected. This is referred to as transport limited sensitivity.

The initial X-ray absorption creates a single free electron (a so-called primary electron); this free electron can then collide with other atoms in the structure causing further ionization while still carrying enough energy to remain in the conduction band. This means that a single X-ray photon absorption event can generate multiple free electrons and holes. The amount of generated charge ΔQ can be related to the amount of absorbed X-ray energy ΔE by

$$\Delta Q = \frac{e\Delta E}{W_{\pm}} \qquad 1.5$$

where $W_{\pm}$ is the electron hole pair creation energy which has been shown by Que and Rowlands [10] to be related to the band gap by $W_{\pm} = 2.2E_g + E_{\text{phonon}}$, where E_g is the bandgap energy and E_{phonon} is a small energy term that represents the involvement of phonons in the EHP creation process. (It not the energy of a single phonon but a term that depends on phonon involvement in the ionization processes.)

1.3.2 Charge transport and Schubweg Limited Sensitivity

To generate an image from the absorbed photons, the generated electron-hole pairs must be separated and drifted to the collecting electrodes from the absorption point without being trapped. The collection efficiency relates the amount of charge generated to the amount of charge that reaches the electrodes (collected). The velocity of this drift is determined by the drift mobility μ and the magnitude of the applied electric field F.

The probability per unit time that a carrier will be trapped in a given trap level in the band gap is determined by the reciprocal of the trapping lifetime τ. Amorphous

selenium contains many localized trapping states within the band gap. Carriers that are trapped as they cross the photoconductor do not contribute to the photocurrent so it is important to design a detector with a high collection efficiency.

The carrier Schubweg is defined as the product of the drift mobility, trapping time (or lifetime), and applied field $\mu\tau F$ and gives the average distance a carrier will travel at a given electric field before being trapped. A thin detector in which $L << \mu\tau F$ would result in a very high collection efficiency; however the X-ray attenuation would be very low. The carrier Schubweg can be directly increased by increasing the applied bias; however this will cause more charge to be injected through the contacts, increasing the dark current and lowering the signal to noise ratio. In practical designs a careful compromise is desired between absorbing as many incident photons (suggesting a thicker layer) and ensuring that the generated charge actually reaches the pixels (suggesting a thinner layer). This leads to a layer with thickness $1/\alpha < L < \mu\tau F$.

1.4 Research objectives

This research focused on the electron transport properties of amorphous selenium (a-Se), for use in direct conversion flat panel X-ray image detectors. Though a-Se has been in use as a photoconductor in flat panel detectors, its structure is still not fully understood. There have been extensive studies of hole transport in a-Se, but the nature of electron transport remains relatively unexplored. Time of flight (TOF) and interrupted field time of flight (IFTOF) techniques were used to characterize a-Se films deposited at the University of Saskatchewan.

1.4.1 Thickness Dependence of Electron Transport

As detailed above, selecting an appropriate photoconductor thickness is a very important step in the design of a digital X-ray image detector. For this study eleven pure a-Se films were deposited and their properties are characterized using TOF experiments to determine electron mobility μ, and IFTOF experiments to determine lifetime τ. These results are plotted as a function of thickness. The result are

expected to be helpful in not only understanding the nature of localized states in a-Se but also in determining the the carrier range $\mu\tau$ as a function of thickness L. The latter would be useful in optimal detector design as $\mu\tau$ controls the charge collection efficiency.

1.4.2 Definitions of Lifetime and Mobility

A detailed explanation of a TOF experiment is included in Section 3. The technique involves creating a nearly uniform sheet of charge just beneath the surface of an a-Se sample and as the charge is drifted across the sample it generates a photocurrent signal in an external circuit. The TOF technique can be used to determine the electron mobility; however it relies on an accurate measurement of electron transit time, which can be defined in multiple ways. This portion of the study explores the effect of the definition of transit time on the calculated mobility.

1.4.3 Dispersive Transport in Pure a-Se

During a TOF experiment, as the charge sheet, is being drifted across the sample it begins to disperse. By the time the carriers reach the bottom electrode, the charge sheet is no longer a uniform thin sheet but a broad distribution. The charge sheet becomes dispersed. There are several reasons for this dispersion, among which are mutual columbic repulsion, carrier diffusion, and multiple trapping and release events. This dispersion is measured and plotted as a function of thickness at various applied fields.

2 Amorphous Selenium

The first successful commercial application of amorphous selenium (a-Se) was in xerography. Xerography's usefulness lead to intensive research of the properties of a-Se during the 1960s and 1970s; however, the advent of personal computing, faxing, and digital document scanning slowed the pace of research as xerography fell out of favour. Indeed a-Se was eventually replaced by organic photoconductors. The suitability of a-Se as an X-ray photoconductor in digital X-ray detectors, on the other hand, has lead to a resurgence in the study of its properties over the last two decades.

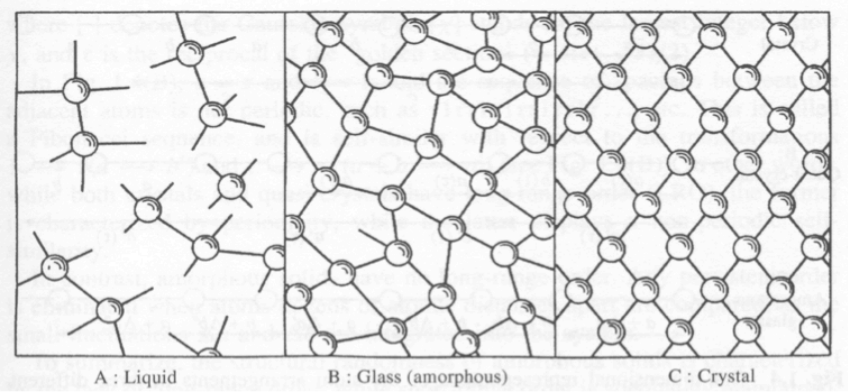

Figure 2.1 A simplified diagram showing atoms arranged in a liquid, amorphous, and crystalline state. An amorphous solid can be thought of a solid that has been frozen in place quickly enough that the atoms did not have time to rearrange themselves into the most thermodynamically favourable state (after Tanaka et al. [12]).

Thermodynamically, amorphous materials can be considered to exist between a liquid state and a crystal state. Figure 2.1 illustrates the lack of long range order and the lack of well defined bond angles in the amorphous and liquid states as compared to a crystal structure. Amorphous semiconductors do not possess long range order; that is, unlike a crystalline semiconductor, given the position of one atom within the structure we cannot precisely predict the position of another atom several atomic distances away from the reference atom. This lack of long range order greatly increases the complexity of analytically describing the properties of amorphous

semiconductors (and, obviously, a-Se) using quantum mechanics. It is possible however to define a density of states (DOS) based band diagram model for amorphous semiconductors and hence for a-Se by combining results of experimental measurements.

2.1 Structure of Amorphous Selenium

Selenium is the 34th element on the periodic table (Z=34) and is a member of the Chalcogens. A Selenium atom has two electrons in the 4s orbital and four in the 4p orbitals, elements in the chalcogen group normally have a p state lone pair in addition to the s state pair, leaving two 4p electrons available for bonding. This leads to a two-fold bonding configuration with an optimum bond angle of 105° [13]. When two covalent bonds are formed in this way, the adjacent atoms share their valence electrons resulting in a more energetically favourable state. By forming two covalent bonds the Se atom has filled its valence shell. In a crystalline structure the number of bonds each atom forms and the angle of those bonds is well defined throughout the material resulting in a periodic structure. In crystalline materials the wave functions of the electrons extend over the entire structure, and the wave functions are described by Bloch waves. We also know that given the position of a single atom one can predict the position of every other atom in the crystal due to the long range order. In an amorphous solid, slight variations in the bond angles and lengths throughout the structure are enough to destroy the periodicity of the network. As only small variations in the bond angle and length are required to destroy this periodicity, the short range order within a few atoms remains similar to that of a crystal and this similarity is sufficient to lead to certain similar electronic properties, one of which is the existence of a band gap.

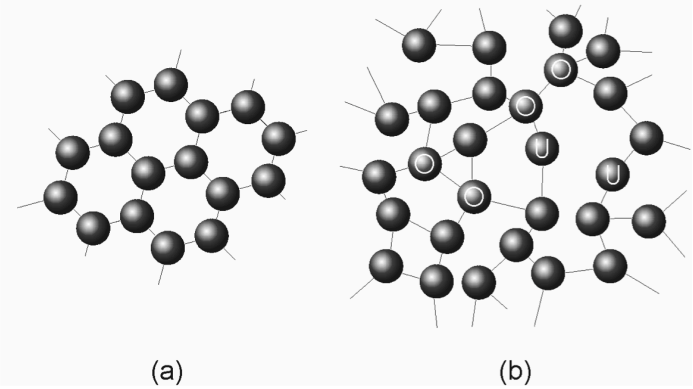

Figure 2.2 A two dimensional comparison of a hypothetical crystalline semiconductor (a) and an amorphous semiconductor (b), note the over (4 bonds) and under (2 bond) coordinated atoms in the amorphous case causing localized defects in the material (after Belev [9]).

Though amorphous semiconductors exhibit many similar properties to their crystalline counterparts, the existence of localized defects such over- and under-coordinated atoms, as shown in Figure 2.2, have a profound impact on their electronic and optical properties.

As mentioned above the ideal bonding scenario for Se is two-fold coordination with a bond angle of 105°. This two-fold coordination results in two crystalline forms: α-monoclinic and γ-trigonal. Monoclinic α-Se is composed of a ring structure of eight Se atoms, while trigonal a-Se consists of spiral chains of Se atoms.

It was initially assumed that a-Se would be composed of a random combination of molecular units from these two crystalline structures scattered throughout the material. However, Lucovsky found that a-Se can be considered to be composed of a random chain model with almost identical bond angle magnitude but randomly alternating sign in the dihedral angle [13-14]. The dihedral angle ϕ is defined in Figure 2.3

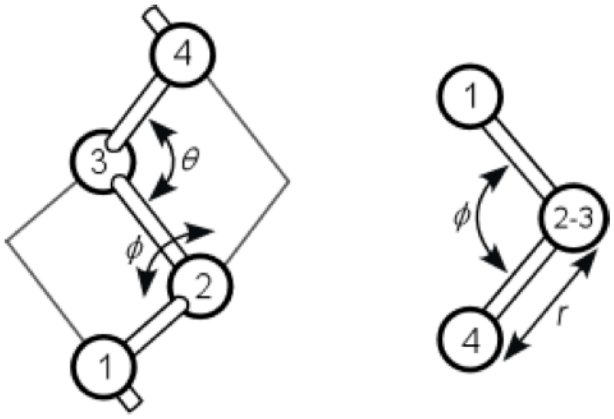

Figure 2.3 Defining the bond angle θ, the dihedral angle ϕ, and the bond length r using a four atom structure to show the random chain model of a-Se (after Kasap [15]).

This leads to areas of the structure that are ring like, or α-monoclinic where the dihedral angle does not change sign and areas that are chain like, or γ-trigonal where the dihedral angle is alternating sign [16], as shown in Figure 2.4.

.

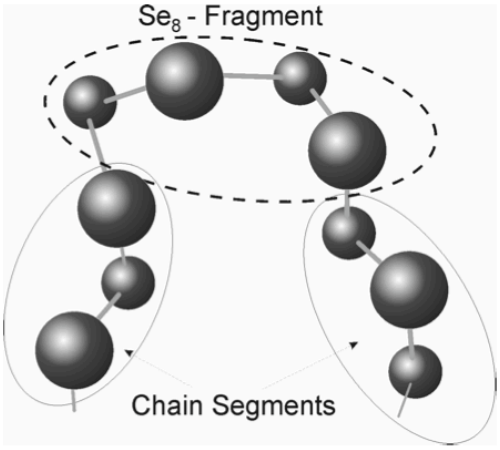

Figure 2.4 A portion of the structure of a-Se, the Se_8 fragment is a ring like structure formed when the dihedral angle ϕ is a constant in that section. The other sections shown are spiral like and form when ϕ is randomly alternating (after Belev [8]).

Defects in the amorphous structure of a-Se are what lead to trailing edges in the energy band diagram. The notation to describe the coordination number of an Se atom is Se_a^b where $1 \leq a \leq 3$ and $b = 0, +, \ or \ -$ .The most energetically favourable

state with twofold coordination is Se_2^0 indicating that the atom has formed two covalent bonds and is therefore electronically neutral. There are many bonding configurations that an Se atom can form including a hyper valency configuration such as SeF_6 where all the 4s and 4p electrons are participating in bonding. It should be noted that the only under-coordinated bonding configuration possible is Se_1 so, when measuring the coordination number of the entire solid, it is expected to be larger than two.

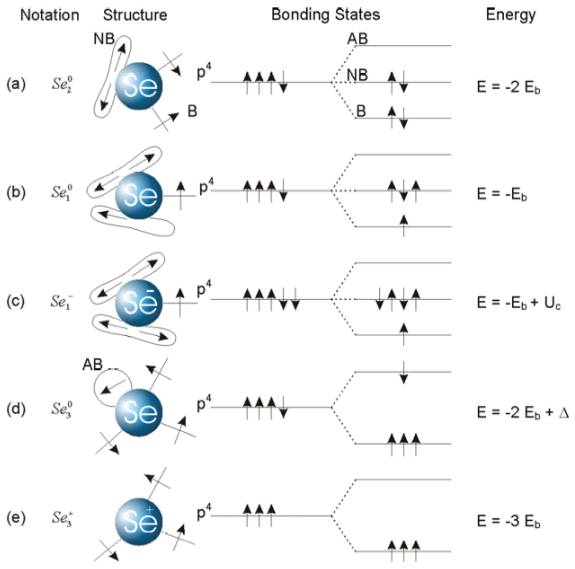

Figure 2.5 Illustration of six simple bonding configurations. In this figure straight lines represent bonds, lobes represent lone pairs and circles represent anti bonding states (adapted from Adler and Yofffa [16]).

Kastner, Adler, and Fritzcshe [17] have concluded that the majority of defects in a-Se take the form of valence alternating pairs; this finding is supported by electronic spin resonance (ESR) studies showing that there are no dangling bonds present in a-Se [18-19]. This lack of dangling bonds means that there are few very neutral defects and the defects must come from over and under-coordinated atoms. A VAP defect is formed in the process.

$$Se_1^0 + Se_2^0 \rightarrow Se_1^- + Se_3^+ \qquad 2.1$$

The process shown in Equation 2.1 is exothermic and occurs when a Se_1^0 atom approaches the 4p orbital lone pair of a Se_2^0 atom. The effect of these IVAP defects in a-Se have been studied extensively and explain several electrical and optical properties of a-Se such as the linear dependence of photoconductivity on light intensity which can be explained by photo induced IVAP defects [20].

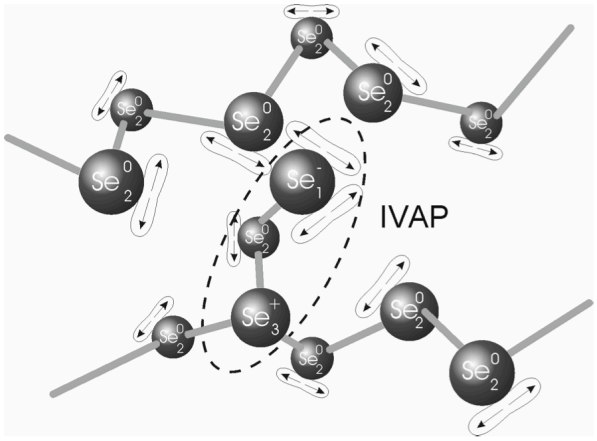

Figure 2.6 Illustration of an IVAP defect in a-Se, note the close proximity of the Se_1^- and Se_3^+ atoms because of their mutual columbic attraction. This distinguishes a valence alternation pair from an intimate (non random) valence alternation pair (after Fogal [2]).

In Figure 2.6, the variations in atomic configuration within the a-Se structure have been described as defects. Due to the lack of long range order in amorphous solids, each atom should therefore take its optimal bonding configuration, which is two bonds per a-Se atom. Structural defects are then variations from this optical bonding configuration. It should be emphasized that, due to the lack of long range order, and the requirement of only optimal bonding per atom, a-Se has no "precisely defined" structure as in its crystalline states [21]. The lack of long range order, and the presence of structural defects such as under- and over-coordinated bonds in a-Se translates to an energy band diagram that is somewhat similar to a crystalline semiconductor but with the addition of localized energy states between the conduction and valence edges. These localized states have a dramatic effect on charge transport in a-Se [22].

2.1.1 Density of States (DOS) for Amorphous Semiconductors and a-Se

Though a-Se has been the subject of extensive study since its suitability as a photoconductor in xerography was first discovered in the 1960's, there remains a significant debate on the exact nature of charge transport in a-Se and therefor the density of states (DOS) model. The DOS model arises from the formation of a semiconducting solid and it is an important concept in understanding the electronic and optical properties of the solid. When we bring together many atoms, each of which has discrete allowable energy levels, the atoms combine to form a nearly continuous band of allowable energy levels. These states are described by the density of states function $g(E)$, defined as the number of allowed energy states per unit of energy, per unit volume. Crystalline semiconductors have a well defined band gap of forbidden states. In order to create a free electron, the latter must gain enough energy to move directly from the valence band into the conduction band. This energy can come from either photons being absorbed, phonons created by lattice vibrations, or collisions with other electrons that have already been moved to the conduction band.

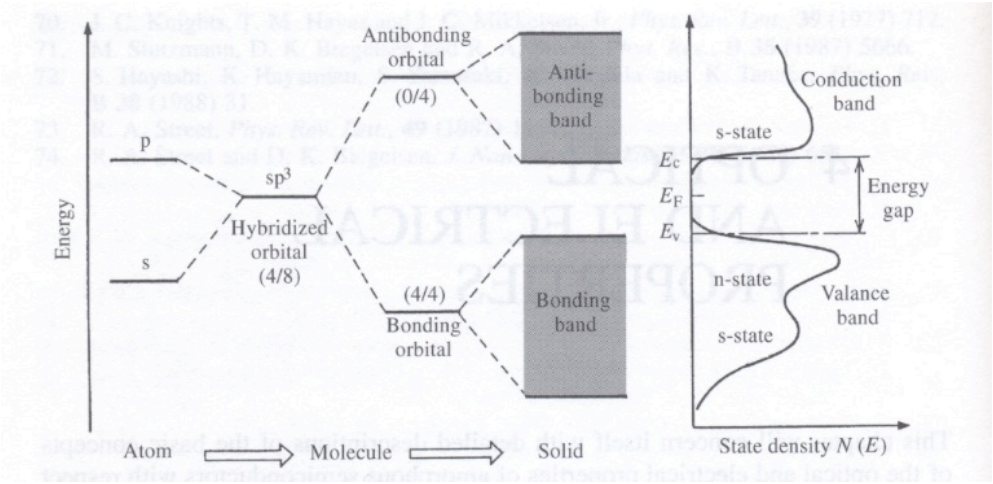

Figure 2.7 The formation of a band gap in a crystalline semiconductor. A strict crystal structure leads to long-range order and a well defined energy gap between the valence and conduction bands. To move into the conduction band an electron must gain at least E_g energy (after Kasap [23]).

The lack of long range order in amorphous semiconductors makes the derivation of a DOS model analytically very difficult as mentioned above. There have been many proposed DOS models over the last fifty years based on various experiments.

Though the exact shape of the DOS curve is still under debate, it has been found that only short range order is required for band theory to be applicable [22]. While the DOS-based band theory can be applied to a-Se, the presence of defects within the structure introduces localized states within the band gap, affecting charge transport. Figure 2.8 shows several of the proposed models from amorphous semiconductors in general; a-Se case is considered later.

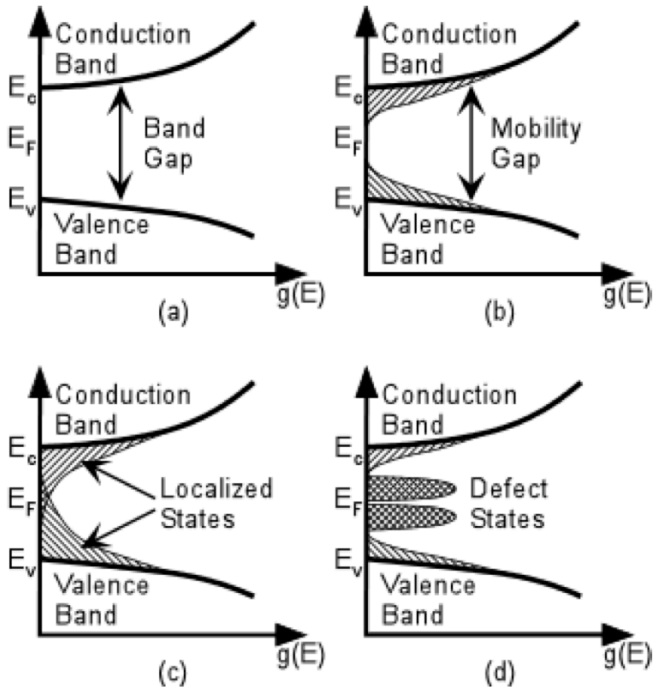

Figure 2.8 Four proposed DOS models for semiconductors. (a) A crystalline semiconductor with well-defined band edges and a band. (b) An initial DOS curve for amorphous semiconductors proposed by Mott [24], the band gap is still present but the conduction and valence band edges have been blurred by the introduction of localized states encroaching into the band gap region. (c) A CFO model [25] where there is a high enough concentration of localized states to extend through the band gap. (d) A DOS model for a-Se proposed by Marshall and Owens [26], this model includes the extended states near the band gap edges as well as two peaks deep within the band gap.

2.1.2 Density of States

The exact shape of the density of states diagram for a-Se remains the subject of much debate; however the most commonly accepted model was proposed by Abkowitz in 1988 [27]. This model combines features from the Owen-Marshall model and data derived from time of flight and other experimental techniques.

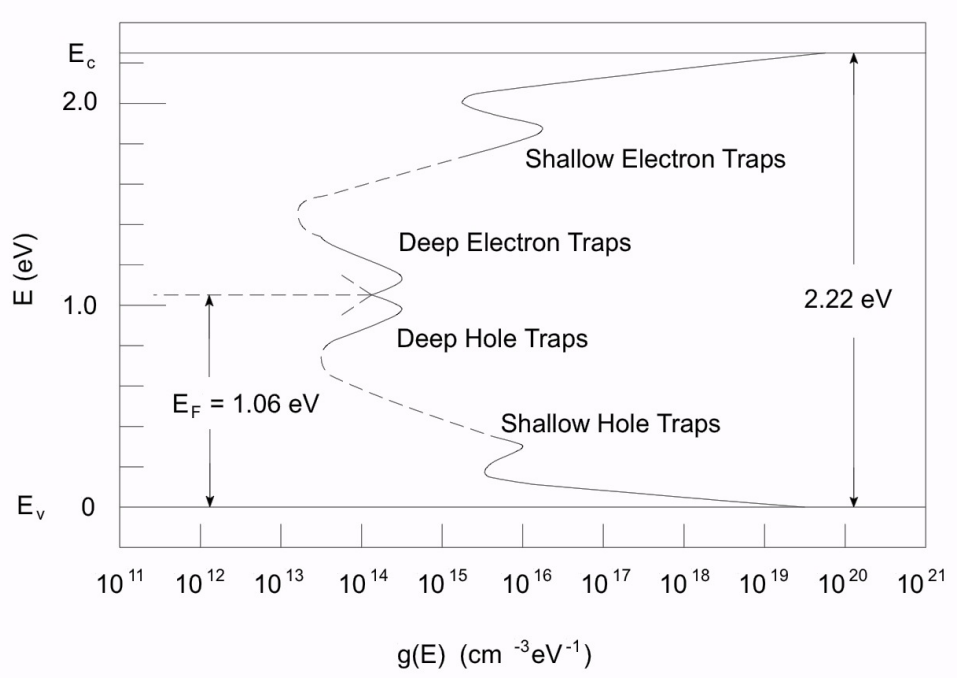

Figure 2.9 Building upon the Marshall Owns model the most widely accepted DOS model for a-Se was proposed in 1988 by Abkowitz et al. Though the band gap is defined as 2.22 eV, optical experiments make this 2.08 eV. This model defines shallow and deep traps for both electrons and holes. These trapping levels are not discrete but rather peaks in an broad distribution that represents the localized carrier traps (localized density of states) throughout the structure (after Abkowitz [27]).

During the early study of a-Se, Spear [28] conducted transit time measurements based on the time-of-flight technique (TOF) at various temperatures and concluded that carrier transport was shallow trap controlled with the shallow traps lying 0.25 eV below the conduction band for electrons and 0.16 eV above the valence band for holes. Thus, it was proposed that both electron and hole transport in a-Se is shallow trap controlled.

Shallow traps reduce the microscopic mobility (μ_o) of a material by a mobility reduction factor θ, so that the effective mobility of the sample μ is given by [20].

$$\mu = \theta\mu_o = \frac{p_{\text{free}}}{p_{\text{free}} + p_{\text{trapped}}}\mu_o \qquad 2.2$$

In equation 2.2, the effective mobility μ of the sample has been reduced because, at any given time during the carrier transit, some of the charge carriers are trapped in shallow traps. It is assumed that under steady state conditions, the concentration of free carriers and the concentration of trapped carriers are in equilibrium.

In the case of a-Se, experiments such that it is useful to consider the shallow and deep traps as consisting of a narrow distribution of states within the band diagram. In the presence of a monoenergetic trap level at an energy E_t below the conduction band, the expression for electron mobility is given by,

$$\mu = \mu_o \left[1 + \frac{N_t}{N_c} \exp\left(\frac{E_t}{kT}\right)\right]^{-1} \approx \mu_o \frac{N_c}{N_t} \exp\left(-\frac{E_t}{kT}\right) \qquad 2.3$$

where μ_o is the mobility within the transport band (conduction band), also called the microscopic mobility, and N_t and N_c are the density of shallow traps (at E_t below E_c) and the effective density of sates at the conduction band edge (at E_c). As the temperature is raised, μ will approach μ_o as $\exp\left(-\frac{E_t}{kT}\right)$ approaches unity. Further, μ_o is diffusional type of transport and has an algebraic temperature dependence of the type $\mu_o \sim T^{-n}$ where $n \approx 1$ [15]. The location of these discrete trap levels can be found by numerically fitting Equation 2.3 to experimentally derived drift mobility vs. Temperature curves. Using this technique, it has been found that $E_t - E_v \approx$ 0.29 eV and $E_c - E_t \approx 0.35$ eV [15]. These points represent the peaks of the shallow traps in a-Se for holes and electrons respectively [29]. Other trap levels, or trap distributions, have been also proposed for a-Se based on various other measurements, for example, from post transit TOF measurements as discussed in the review by Kasap and Rowlands in reference [8].

To determine the location of the deep trap peaks, Abkowitz used the photoinduced discharge and cycled up xerographic residual voltage methods. These experiments indicated a deep trapping level for holes 0.87 eV above E_v and a deep trapping level

for electrons 1.22 eV below E_c. In Section 3 this binary trap distribution model will be used to derive an expression for electron transport in a-Se.

In the case of a-Se, there is much evidence that the localized states in the band gap of a-Se are thermodynamically stable structural defects in the structure. Though the exact structure of these defects remains unknown, it is commonly accepted that they are related to valence alternation pair (VAP) defects [8,15,18]. Introducing ppm amounts of impurities can have a drastic effect on the charge transport properties of a-Se. In practice, pure selenium is not used in detector applications as it crystalizes much too quickly so between 0.2-1% As is introduced to prevent the crystallization. This material, a-Se:(0.2-1)%As + a few ppm Cl, is referred to as *stabilized amorphous selenium*; stabilized a-Se

2.1.3 Optical Properties of a-Se

The original discovery of the photoelectric effect by Willoughby Smith in the late 19th century came from his observation that the resistivity of Selenium rods decreased drastically when they were illuminated by a strong light source. He published his findings titled "Effect of Light on Selenium during the passage of an Electric Current" [32] in Nature. Photoconductivity describes the phenomenon where an incident photon is absorbed within the material exciting an electron across the bandgap, therefore increasing the free carrier density. The probability that an incident photon will be absorbed and excite an electron depends on the optical absorption coefficient α of the material, which is a function of photon energy and the joint density of states at the band edges. Photons with energy less than the band gap have a very low (nonzero) probability of being absorbed. These lower energy photons can still excite electrons that have been trapped in the localized states within the bandgap. This behaviour is characterized by an Urbach edge [34].

$$\alpha(hv) = 7.35x10^{-12} \exp\left(\frac{hv}{0.058\ \text{eV}}\right) \text{cm}^{-1} \qquad 2.4$$

At photon energies greater than the optical bandgap, absorption increases drastically. For a-Se the optical bandgap E_o is approximatrely 2.08 eV; smaller than the band gap of 2.22 eV from electrical measurements.

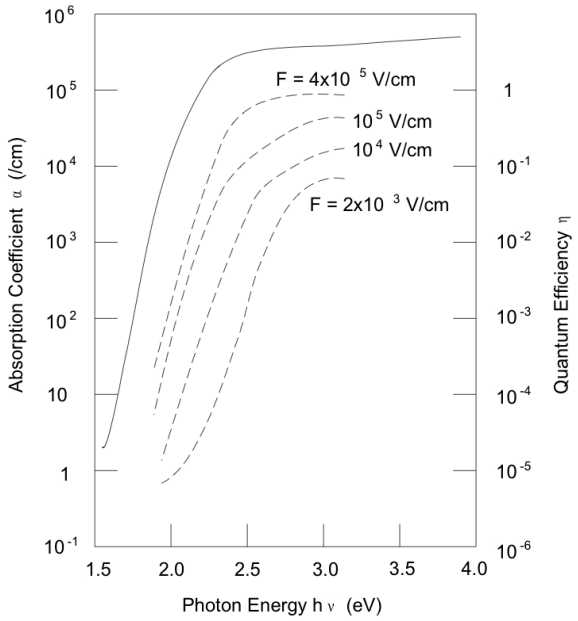

Figure 2.10 Absorption efficiency α (solid line) and quantum efficiency η (dashed line) for a-Se are plotted as a function photon energy (*hν*) (after Pai [34]).

After a photon is absorbed and creates an electron hole pair, the probability that the pair will separate and drift the carriers across the material is given by the quantum efficiency η, which depends on the temperature and applied electric field. Quantum efficiency in a-Se has been shown to exhibit a strong field dependence even when the incident photons have energy much greater than the band gap [34]. If the EHPs are not separated after absorption of the photon they will be lost and not contribute to the final image.

The field dependence of η can be explained by the Onsager theory for disassociation of EHPs [34] which, given an applied electric field and temperature, calculates the probability that an EHP will diffuse apart. Using this theory, the quantum efficiency can be calculated as $\eta = \eta_o f(F, T, r_o)$ where η_o is the intrinsic quantum efficiency of the material, $f(F, T, r_o)$ is the probability that the pair will separate and r_o is the separation of the EHP immediately following absorption.

The combination of the absorption coefficient α and quantum efficiency η is a very important factor in the design of a photodetector. Increasing the a-Se layer thickness will increase the proportion of incident photons that are absorbed but the electric field will also need to be increased to maintain η which also increases the dark current, lowering the signal to noise ratio. Although the above discussion addressed optical absorption α and optical photogeneration efficiency η, the X-ray photogeneration efficiency also depends on the electric field [10].

2.2 Summary

This section provided an overview of the structure and properties of amorphous selenium. The basic notions such as the density of states (DOS) from semiconductor science can be applied as a useful concept in understanding the properties of a-Se; however deriving the actual DOS analytically has proven very difficult due to the lack of long range order in the structure. This has led to decades of research to derive the density of states (DOS) experimentally. The most commonly accepted DOS for a-Se as proposed by Abkowitz was presented. To derive this DOS, possible bonding configurations within the structure were explored. The localized tail states near the band edges are caused by random variations in the bond angles of twofold coordinated Se atoms or random variations in the dihedral angle of twofold coordinated Se atoms. The deep traps are likely to be caused by valence alternation pair (VAP) defects.

In the case of a-Se, it is believed that the existence of allowable localized states within the bandgap is due to thermodynamically derived defects at room temperature. Currently accepted view of charge transport in a-Se is that the shallow trapping levels control the carrier mobility (multiple trapping and release events during the transit time), while the deeper trapping levels control the carrier lifetime (no observable release during the transit of the carriers). Though this is the most commonly accepted model, evidence of a third intermediate level of traps exists and the exact nature of the DOS curve remains the subject of much debate [8]. Time of

flight and interrupted field time of flight photoconductivity techniques can be used to determine carrier mobility and lifetime; and are probably the best suited experimental techniques for studying a-Se. Chapters 3 and 4 provide the necessary theoretical background and the experimental procedure for carrying out these experiments.

3 Time of Flight, Interrupted Field Time of Flight Transient Photoconductivity

3.1 Introduction

The complex and nonperiodic structure of amorphous semiconductors makes an analytical derivation of the density of states (DOS) model very difficult. This difficulty has lead many researchers to use experimental techniques to extract the DOS; two important techniques for analyzing these materials are the time of flight (TOF) and interrupted field time of flight (IFTOF) photoconductivity techniques. This section presents a description of TOF and IFTOF methods, including detailed descriptions of the system used in this study. Also included is the experimental procedure used to determine the thickness dependence of electron transport in pure amorphous selenium.

3.2 Time of Flight Transient Photoconductivity Experiment

The time of flight transient photoconductivity technique is used to determine charged carrier mobility in highly resistive materials by observing the transient response of a sheet of charge injected into the material. The basic schematic shown in Figure 3.1 illustrates the TOF technique for a trap free solid.

The basic requirements for performing a TOF experiment are a sample to be measured sandwiched between two non-injecting metal electrodes, a voltage source to apply bias across the sample, a light source capable of generating a very short duration pulse, a sampling resistor to measure the transient photocurrent, and an amplifier connected to a readout device for recording the TOF signal.

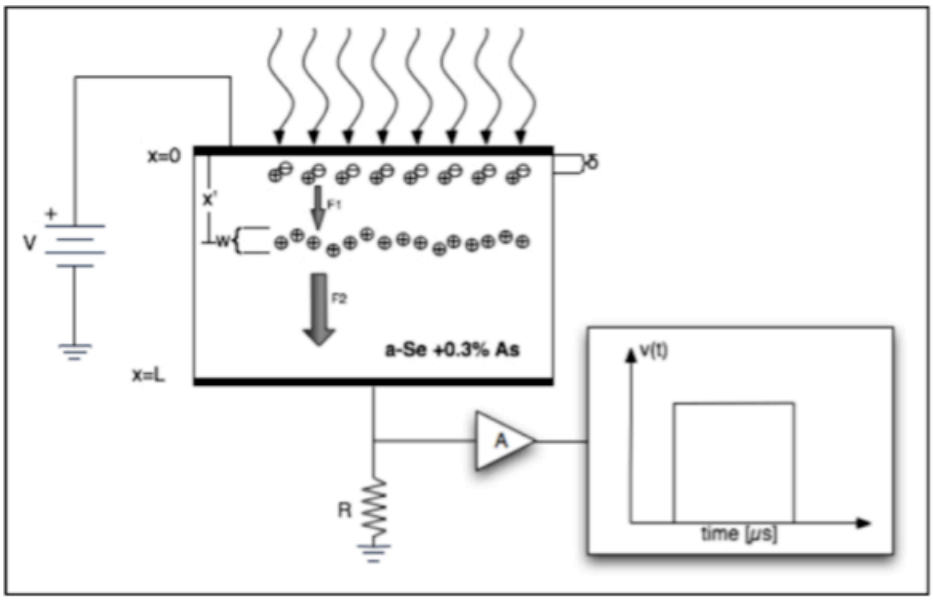

Figure 3.1 Basic TOF system diagram showing; applied bias to drift carriers, illumination and absorption within the absorption depth ($\delta = 1/\alpha$), carrier drift due to applied field, sampling resistor, amplification, and the measured TOF signal for a trap free perfect solid under small signal conditions.

To begin the experiment, the voltage source is switched on, creating an electric field across the sample, because the sampling resistor is chosen to have resistance much smaller than the sample ($R_{\text{sample}} \gg R$); almost the entire applied field appears across the sample.

The sample is then subjected to a very short duration pulse of light such as that given by a xenon flash or nitrogen pumped laser. The wavelength of this illumination is chosen to ensure that the absorption depth δ will be negligibly small compared to the sample thickness L; $\delta << L$. This simplifies the analysis as the holes can be considered to be traversing the entire thickness L of the sample while the electrons will be almost immediately absorbed by the top electrode.

After the electrons have been neutralized by the top contact there remains a distribution of holes within the absorption depth δ. We can simply take this distribution as a sheet of holes since $\delta << L$. This charge sheet begins to drift across the sample under the influence of the applied electric field F. As the charge sheet drifts across the sample some of the carriers experience multiple trapping and release events in shallow traps, while some of the carriers will be trapped in deep

traps and lost for the duration of the experiment. In this way, the shallow trapping levels limit the carrier mobility, and the deep traps determine the carrier lifetime. The moving sheet of charge generates a current $\mathrm{i_{ph}}(t)$ in the external sampling resistor *R*; the voltage across this sampling resistor is then amplified and displayed on an oscilloscope or saved to a personal computer.

To understand the mechanism that generates the external current i_{ph} we consider the charge sheet to be laterally uniform as it traverses the sample. Under small signal conditions, this charge sheet will not significantly modify the total internal field; however there will be a difference in electric field on either side of the charge sheet. These two electric fields F_1 and F_2 are dependent on the position of the charge in the sample and can be calculated by [28]

$$F_1 = F_o + \frac{ep_o w}{\epsilon}\left(\frac{x'}{L} - 1\right) \qquad 3.1$$

$$F_2 = F_o + \frac{ep_o w}{\epsilon}\, x'/L \qquad 3.2$$

where *e* is the charge of an electron, p_o is the concentration of carriers (holes) in the charge packet, *w* is the width of the charge packet, *x'* is the distance the packet has travelled through the sample, ϵ is the permittivity of the medium (the product of absolute permittivity and relative permittivity), and *L* is the thickness of the sample.

Equations 3.1 and 3.2 represent the electric field on either side of the charge sheet at *x'* at any position throughout the sample. These equations show that, as the charge crosses the sample, the applied field $F_o = V_o/L$ is modified and F_1 is reduced while F_2 is increased slightly. This slight difference between the electric fields must induce a current i_{ph} in the external circuit, which flows through the sampling resistor to be amplified and displayed.

The small signal condition of a TOF experiment specifies that the moving charge has a negligible effect on the applied field, $\frac{en_o w}{\epsilon} \ll \frac{V_o}{L}$. Under this condition, the drift velocity of the charge packet through the sample can be assumed to be constant [36]. The small signal condition greatly simplifies the photocurrent analysis; when it is not met, the space charge effect on the electric field must be taken into account [36].

Using the Ramo-Shockley Theorem [23], the instantaneous current *i* is given by $i = E_v q v$ where E_v is the electric field at the position of the charge, q is the amount of charge and v is the instantaneous velocity of the charge. Using the Ramo-Shockley Theorem, we can easily derive an expression for the magnitude of the induced photocurrent in the external circuit [23].

The total charge injected into the sample by the light source is $Q_o = ep_o wA$ where e is the charge of an electron, p_o is the concentration of charge carriers, w is the width of the charge sheet, and A is the area of the charge sheet. From the Ramo-Shockley theorem, the instantaneous photocurrent is given by

$$i_{\text{ph}} = \left\{\frac{q v_d(t)}{L}\right\} \text{ when } 0 < t < t_T \qquad 3.3$$

$$i_{\text{ph}} = 0 \text{ when } t > t_T \qquad 3.4$$

Equations 3.3 and 3.4 show that the photocurrent is only present while the carriers are traversing the sample, after the charge sheet reaches the bottom electrode the photocurrent drops to zero; this time is defined as the *transit time* t_T. Provided that the small signal condition is met,

$$t_T = \frac{L}{v_d} = \frac{L^2}{\mu V_o} \qquad 3.5$$

where μ is the drift mobility of the photoinjected and drifting carriers (holes in this example). To determine the voltage signal observed across the sampling resistor R, as a result of the induced photocurrent flowing through it, we consider the ac equivalent circuit of the sample and sampling resistor.

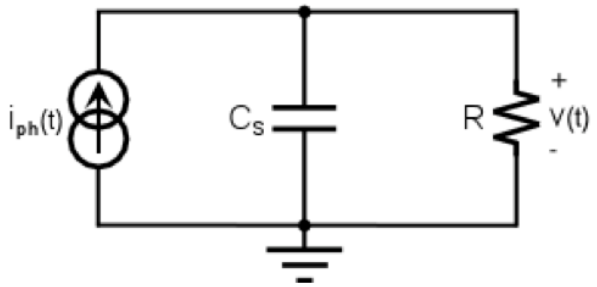

Figure 3.2 AC equivalent circuit of the sample C_s, sampling resistor R, and induced photocurrent i_{ph} showing the voltage response $v(t)$ across the sampling resistor.

Taking the Laplace transform of the circuit shown in Figure 3.2 and rearranging it, it can be shown that

$$V(s) = \frac{R}{sRC_s + 1} I_{\text{ph}}(s) \qquad 3.6$$

The inverse Laplace transform of Equation 3.6 can yield two asymptotic and convenient solutions depending on the relationship between RC_s and t_T. I f $RC_s \ll t_T$, and the bandwidth of the photocurrent is defined as $\sim 1/t_T$, then,

$$v(t) \approx Ri_{\text{ph}}(t) \text{ when } 0 < t < t_T \qquad 3.7$$

$$v(t) = 0 \text{ when } t > t_T$$

The expression in Equation 3.7 is called the I-mode signal. The signal rises quickly when the charge is injected, remains at a value proportional to the photocurrent while the carriers traverse the sample, and drops to zero immediately after the carriers reach the bottom collecting electrode. The second solution to the inverse

Laplace transform of Equation 3.6 occurs when $RC_s \gg t_T$, and is referred to as the V-mode signal.

$$v(t) \approx \frac{\frac{1}{C_s} ep_o wA}{t_T} t \qquad \text{when } 0 < t < t_T \tag{3.8}$$

$$v(t) \approx \frac{1}{C_s} ep_o wA \qquad \text{when } t > t_T$$

which simplifies to,

$$v(t) \approx \frac{1}{C_s} \int_0^t i_{ph}(t')dt' \qquad \text{for } RC_s \gg t_T \tag{3.9}$$

The V-mode signal begins at zero when the charge is just injected and rises linearly as the charge sheet is drifted across the sample to a value proportional to the total charge injected into the sample. It is an integral of the photocurrent. The V-mode signal is useful for measuring the total charge injected, as its final value is proportional to the charge. The V-mode has one distinct advantage. Due to the integration involved, the noise in the measurement is reduced and the signal to noise ratio is generally better than that in the I-mode measurement. The I-mode and V-mode signals in Equations 3.7 and 3.9 respectively have assumed a trap free solid, that is, as the charge sheet crosses the sample none of the charge is impeded by localized states within the solid. As we know from Chapter 2, this assumption is not valid in amorphous selenium because there are many localized states within the band gap. As these trapping states are added to the analysis of charge transport, the interpretation of the TOF experiments becomes correspondingly more complex. The following considers the case where only deep traps are present.

Deep traps in a semiconductor are classified as those traps that essentially remove carriers from the charge packet without releasing any back into the transport band, over the time scale of observation. All such traps can be characterized by a mean

trapping time τ_c which is the average time a carrier can be free in the solid before be trapped. For deep traps, it is assumed that the release time τ_r is much longer than the transit time; therefor carriers captured in deep traps are remove from the charge sheet and cease contributing to the photo current. This trapping introduces an exponential decay to the photocurrent throughout the transit time. Taking this into account Equation 3.3 becomes,

$$i_{ph}(t) = \frac{ep_o wA \exp\left(-\frac{t}{\tau_c}\right)}{t_T} \qquad 3.10$$

Substituting Equation 3.10 into Equation 3.7 yields an expression for the I-mode current with deep traps,

$$v(t) = R\frac{ep_o wA \exp\left(-\frac{t}{\tau_c}\right)}{t_T} \text{ when } 0 < t < t_T \qquad 3.11$$

$$v(t) = 0 \text{ when } t > t_T$$

Integrating Equation 3.11 leads to an expression for the V-mode current with deep traps as

$$v(t) = \frac{ep_o wA\tau_c}{C_s t_T}\left(1 - \exp\left(-\frac{t}{\tau_c}\right)\right) \text{ when } 0 < t < t_T \qquad 3.12$$

$$v(t) = \frac{ep_o wA\tau_c}{C_s t_T}\left(1 - \exp\left(\frac{t_T}{\tau_c}\right)\right) \text{when } t > t_T$$

Equation 3.12 is known as the Hecth relationship [37], and can be used to estimate the trapping time from TOF signals.

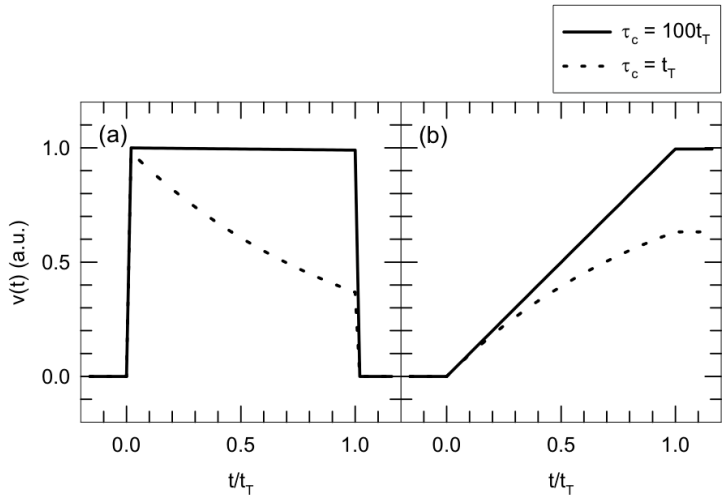

Figure 3.3 Expected I-mode and V-mode signals with and without deep traps. Note the exponential decay of the photocurrent signal when deep traps are added, and that the V-mode signal is the integral of the I-mode signal (after Fogal [2]).

Comparing the idealized I-mode signal of Figure 3.3a to a typical example for a-Se in Figure 3.4 reveals several differences. The captured signal exhibits a long tail due to charge sheet dispersion during the transit time as well as multiple trapping and release events in shallow traps. The simplified explanation above of the TOF signal in the presence of deep trapping neglected the effects of shallow traps and the charge packet dispersion during drift.

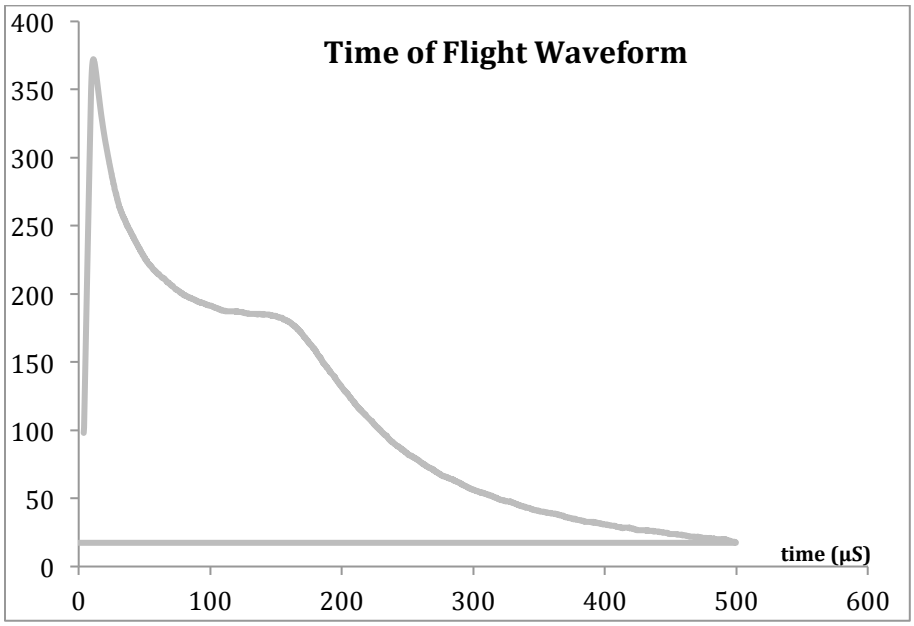

Figure 3.4 A captured TOF I-mode signal for electron transport in a stabilized a-Se sample.

3.3 Interrupted Field Time of Flight Transient Photoconductivity Experiment

The interrupted field time of flight (IFTOF) technique can used to determine deep trapping lifetimes in highly resistive materials. An IFTOF experiment begins in the same manner as a TOF experiment. However, after delay time $0 < t_d < t_T$ the high voltage bias is switched off leaving the charge sheet stationary inside the sample, causing the induced photocurrent to drop to zero, until the voltage is switched back on after some interruption time t_i and the carriers continue to traverse the sample. During the interruption time, some of the carriers will be captured in deep traps at the location $l = t_d L/t_T$. Therefore, when the voltage is switched back on, the photocurrent will have diminished. By observing the difference between photocurrent before and after interruption, and assuming a well-defined capture time τ_c, the charge carrier concentration before and after interruption can be expressed by,

$$\frac{n(t_2)}{n(t_1)} = \exp\left(-\frac{t_i}{\tau_c}\right) \qquad 3.13$$

Since the photocurrent is directly proportional to the concentration of carriers in the charge packet under small signal conditions, the magnitude of the photocurrent before $i(t_1)$ and after $i(t_2)$ interruption are related by

$$\frac{i(t_2)}{i(t_1)} = \exp\left(-\frac{t_i}{\tau_c}\right) \qquad 3.14$$

The difference in photocurrents due to trapping is illustrated in Figure 3.5

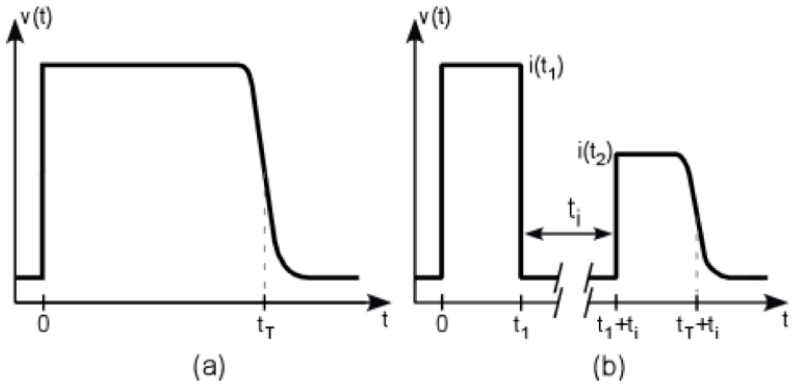

Figure 3.5 Conventional TOF (a) and IFTOF (b) waveforms, during the interruption time $t_i = t_2 - t_1$ some carriers are trapped in deep traps, therefor the current following interruption is less than that before interruption, the relationship between $i(t_2)$ and $i(t_1)$ can be used to estimate the deep trapping lifetime τ_c (after Allen [6]).

To determine the carrier lifetime, multiple IFTOF experiments are performed at the same location within the solid ($l = t_d L/t_T$), while varying the interruption time t_i The fractional recovered photocurrent $i(t_2)/i(t_1)$ can be plotted against the interruption time on a semi logarithmic graph, the slope of which is determined by the deep trapping carrier lifetime τ_c.

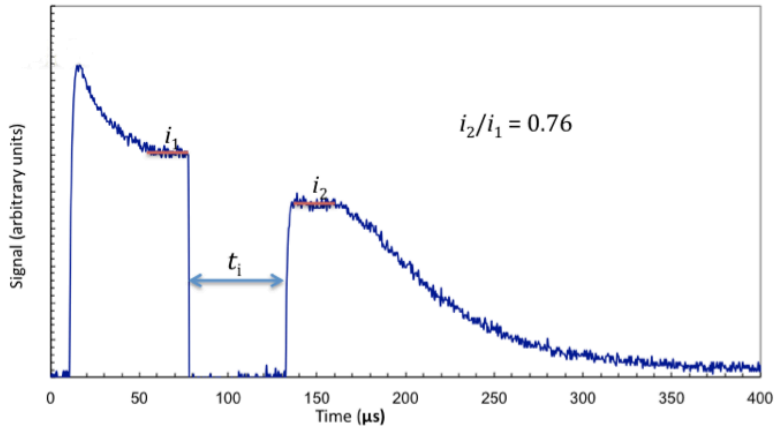

Figure 3.6 A captured IFTOF waveform with delay time 80 µs and interruption time of 50 µs, note the difference between i_2 and i_1 in this case $\frac{i_2}{i_1} = 0.76$.

Figure 3.6 shows an example of an IFTOF experiment in which $i(t_2)/i(t_1)$ =0.76. By performing multiple IFTOF experiments while varying the interruption time, and plotting the data on a semi logarithmic graph, the lifetime can be readily determined as shown in Figure 3.7.

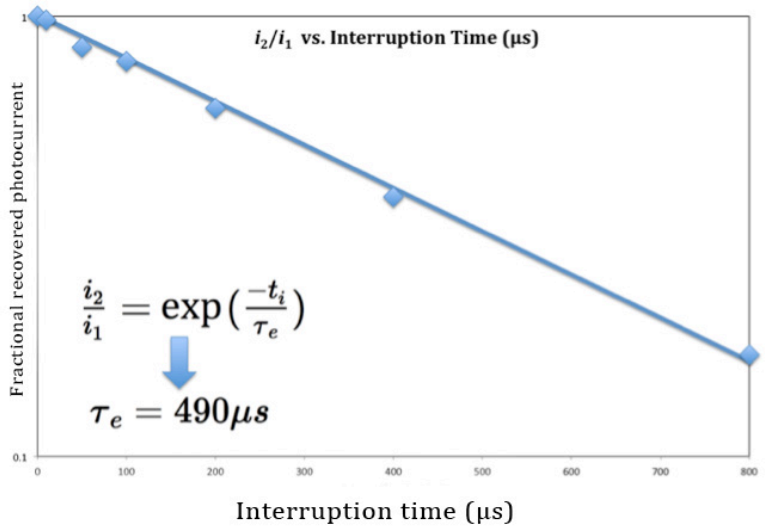

Figure 3.7 Determining the carrier deep trapping lifetime from multiple IFTOF experiments, in this case $\tau_e = 490$ μs.

3.4 Time of Flight Transient Photoconductivity with Trapping

The previous derivations assumed either a trap free solid, or a solid with only deep trapping levels, neither of these assumptions can be used to properly describe the transient response of a-Se to the photoinjection of charge such as in a TOF experiment or its use as a practical detector. The following section details three more realistic scenarios for modeling the response of a-Se. These are a monoenergetic trap level near the band edge, a binary trap distribution, which includes shallow and deep traps, and finally a continuous trap distribution throughout the band gap.

3.4.1 Discrete Monoenergetic Trap Distribution Near the Conduction Band

In this section an expression for the flow of electrons in a solid with a discrete set of traps near the conduction band edge is developed. The localized states near the conduction band will temporarily remove electrons from the charge sheet, hold them for some time, and then release them back into the conduction band. These traps are referred to as shallow traps because the carriers trapped at this level are not lost from the photocurrent, only temporarily removed until a lattice vibration excites the electron back into the conduction band. To develop the appropriate expression we must consider the concentration of carriers within an infinitesimally small slice of thickness *dx* in the solid. The quantity of free electrons in this slice will

change due to free electrons flowing through the slice, electrons being trapped, and electrons being released from deep traps. This relationship is expressed in Equation 3.15 where $J(x,t)$ is the current density, $n(x,t)$ is the free electron density at some position *x* at time *t* within the solid, and $n_t(x,t)$ is the concentration of trapped electrons at position *x* and time *t*.

$$\frac{\delta n(x,t)}{\delta t} = -\frac{1}{e}\frac{\delta J(x,t)}{\delta x} - \frac{\delta n_t(x,t)}{\delta t} \qquad 3.15$$

The current density at any point in the solid is comprised of two parts, which are in opposition with each other. The first component is the electrons being drifted by the applied voltage, this is called the conduction current, the second part is caused by the spatial variation of carriers in the charge sheet, and this component is called the diffusion current. The conduction current J_C is given by,

$$J_c(x,t) = e\mu_o n(x,t)F(x,t) \qquad 3.16$$

where *e* is the charge of an electron, μ_o is the mobility of the electrons in the transport band, $n(x,t)$ is the concentration of free electrons, and $F(x,t)$ is the electric field at position *x* and time *t*. The diffusion current component J_D is much smaller and given by

$$J_D(x,t) = -\frac{eD\delta n(x,t)}{\delta x} \qquad 3.17$$

The total current density is the sum of drift and diffusion currents and is given by,

$$\frac{\delta n(x,t)}{\delta t} = \mu_o F(x,t)\frac{\delta n(x,t)}{\delta x} + \mu_o n(x,t)\frac{\delta F(x,t)}{\delta x} + D\frac{\delta^2 n(x,t)}{\delta x^2} - \frac{\delta n_t(x,t)}{\delta x} \qquad 3.18$$

Equation 3.18 is referred to as the one dimensional continuity equation for electrons, $n_t(x,t)$ is the concentration of electrons in shallow traps. If the small signal condition ($\frac{en_oW}{\epsilon} \ll \frac{V_o}{L}$) is met the diffusion current can be assumed to be negligible and the electric field $F(x,t)$ can be assumed to be constant.

The following derivation yields an expression for the time dependence of electron concentration during a TOF experiment where the sample is subjected to a delta input of light, causing excitation of a sheet of electrons just inside the top of the sample. These electrons will be drifted across the sample by the applied bias while interacting with the shallow traps near the conduction band.

At time t = 0 a short light pulse creates a sheet of charge, the concentration profile of this charge sheet is assumed to be a delta function given by,

$$n(x,0) = N_o\delta(x,0) \tag{3.19}$$

where N_o is the number of electrons initially generated, it is assumed that at the beginning of the experiment none of the traps are filled with electrons so,

$$n_t(x,0) = 0 \text{ for } x > 0 \tag{3.20}$$

There are also no electron traps outside the sample so $n_t(x,t) = 0$ for $x > L$ and the free electron density outside of the sample is also assumed to be 0 so that $n(x,t) = 0$ for $x > L$. The following expression for free electron density can be found by using the boundary conditions above, and Laplace transforms as described in [39-40].

$$\begin{aligned} n(x,t) = {} & \frac{N_o}{\mu_o F}\exp\left(-\frac{z}{\tau_c}\right)\delta(t-z) \\ & + \frac{N_o}{\mu_o F}\exp\left[-\frac{z}{\tau_c}-\frac{t-z}{\tau_r}\right]\frac{\xi}{2}\frac{I_1(\xi)}{t-z}U(t-z) \end{aligned} \tag{3.21}$$

where $z = \frac{x}{\mu_o F}$, $I_1(\xi)$ is a first order hyperbolic Bessel function, $U(x)$ is the unit step function $\xi = \frac{2\sqrt{\tau_c z(t-z)}}{\sqrt{\tau r}} / \tau_c$ and $\frac{N_o}{\mu_o F} \exp\left(-\frac{z}{\tau_c}\right) \delta(t-z)$ is the number of free electrons still in the conduction band. Breaking apart Equation 3.21, the first term represents the free carriers that have not interacted with traps. This term decreases exponentially as the charge packet crosses the sample as electrons are trapped in deep traps. The second term (containing the Bessel function) represents the carriers that have been trapped in shallow traps and released - these carriers lag behind the charge packet and are part of the reason for the tail in a real world TOF experiment.

Integrating Equation 3.21 over the entire length of the sample would lead to an expression for the number of free electrons at any given time, however this is a nontrivial integration. So, instead, Equation 3.21 is evaluated for two limiting cases; high field drift and low field drift.

In the case of low field drift, the transit time t_T is much longer than the mean free capture time τ_c. This means that within the transit time the number of carriers occupying the shallow traps and those being released from shallow traps will reach equilibrium. As this relationship reaches equilibrium, the time derivative of the trapped carrier density will go to zero [30, 31]. In the low field condition, the carriers experience multiple trapping and release events as they cross the sample. After equilibrium is reached, the number of free electrons will be given by,

$$N = N_o \frac{\tau_c}{\tau_c + \tau_r} \qquad 3.22$$

where N is the number of free electrons, N_o is the total number of electrons injected, τ_c is the mean free capture time, and τ_r is the mean release time from the shallow traps. As this model considers a monoenergetic trap level, τ_c and τ_r are well defined.

Given the number of free electrons, the external photocurrent is derived by substituting Equation 3.22 into Equation 3.6.

$$i_{ph} = \frac{eN_o\mu_o F}{L}\frac{\tau_c}{\tau_c + \tau_r} = \frac{eN_o\mu F}{L} \qquad 3.23$$

where

$$\mu = \mu_o \frac{\tau_c}{\tau_c + \tau_r} = \theta\mu_o \qquad 3.24$$

Equation 3.24 shows that in the case of a monoenergetic trap level near the conduction band the effective mobility of the solid is reduced by $\theta = \tau_c/(\tau_c + \tau_r)$. This case is referred to as shallow trap controlled transport where the shallow trap level limits the carrier mobility within the solid.

The high field case differs in that some of the carriers will cross the sample without interacting with the shallow traps, $L/\mu_o F \ll \tau_c$. Martini et al. [30] have developed an expression to describe this case under two different time ranges $0 < t < L/\mu_o F$ and $t > L/\mu_o F$; these are shown in Equations 3.25 and 3.26 respectively.

$$i_{ph}(t) = \frac{eN_o}{\tau_T}\left[\frac{\tau_c}{\tau_r + \tau_c} + \frac{\tau_r}{\tau_r + \tau_c}\exp\left(-\frac{\tau_c + \tau_r}{\tau_c\tau_r}t\right)\right] \text{ when } 0 < t < \frac{L}{\mu_o F} \qquad 3.25$$

$$i_{ph}(t) = \frac{eN_o}{2}\frac{t_T}{\tau_r\tau_c}\exp\left(-\frac{t}{\tau_r}\right) \text{ when } t > \frac{L}{\mu_o F} \qquad 3.26$$

Equation 3.26 represents those carriers that have been trapped in a shallow trap and released at some later time. In the high field case, these carriers are not likely to be trapped again before reaching the bottom electrode. This equation represents the

exponential decay to zero as those carriers that have been trapped and released exit the sample after a step change when the first group of electrons reaches the bottom electrode.

3.4.2 Binary Trap Distribution Model

Section 3.4.1 developed an expression for electron transport during a TOF experiment assuming a discrete set of shallow traps at one energy level and correspondingly one mean free capture τ_c and release time τ_r. This section extends this analysis by adding a deep trapping level and develops an expression involving two capture times τ_{c1} and τ_{c2} and two release times τ_{r1} and τ_{r2} along the lines described in [31]. To simplify the analysis, it is assumed that no carriers move between the two trapping levels directly; that is, an electron does not move from the deep trapping level to the shallow trapping level without passing through the conduction band. Equations 3.27 and 3.28 show the electron rate equations for a binary trap distribution,

$$\frac{\delta n_{t1}(x,t)}{\delta t} = \frac{n(x,t)}{\tau_{c1}} - \frac{n_{t1}(x,t)}{\tau_{r1}} \qquad 3.27$$

$$\frac{\delta n_{t2}(x,t)}{\delta t} = \frac{n(x,t)}{\tau_{c2}} - \frac{n_{t2}(x,t)}{\tau_{r2}} \qquad 3.28$$

The following final result was derived by Blakney and Grunwald [31] regards the binary trap distribution as the superposition of two exponentially decaying components so that the photocurrent is given by

$$j(t) = A\exp(-\alpha t) + B\exp(-\beta t) + j_\infty \qquad 3.29$$

$$\alpha + \beta = \frac{1+\theta_1}{\tau_{c1}} + \frac{1+\theta_2}{\tau_{c2}} \qquad 3.30$$

$$\alpha\beta = \frac{[\theta_1 + \theta_2(1+\theta_1)]}{\tau_{c1}\tau_{c2}} \qquad 3.31$$

$$\alpha A + \beta B = \frac{j_o}{\tau_{c1}} + \frac{j_o}{\tau_{c2}} \qquad 3.32$$

$$A + B + j_\infty = j_o \qquad 3.33$$

$$j_\infty = \frac{j_o \theta_1 \theta_2}{[\theta_1 + \theta_2(1 + \theta_1)]} \qquad 3.34$$

$$\theta_1 = \frac{\tau_{c1}}{\tau_{r1}} \text{ and } \theta_2 = \frac{\tau_{c2}}{\tau_{r2}} \qquad 3.35$$

This derivation uses j_∞ for the steady state current when the number of carriers being trapped and released by all the traps has reached equilibrium. In the case of TOF experiments with a-Se, the deep trapping levels do not release carriers back into the conduction band within the timeframe of the experiment ($\tau_{r2} \rightarrow \infty$) and $\theta_2 = 0$. Equation 3.29 reduces to Equation 3.36, which is known as *shallow trap controlled transport with deep trapping*. This approximation is very useful in the analysis of a-Se as it closely mirrors the density of states model proposed by Abkowitz and described in Section 2.

$$j(t) = A\exp\left(-\frac{t}{\tau_{c1}}\right) + B\exp(-\frac{\theta_1 t}{\tau_{c2}}) \qquad 3.36$$

3.4.3 Extended Trap Distribution Model

Compared to the monoenergetic and binary trap distribution models, developing an analytic expression for the transient trap limited response of a-Se with an extended (continuous) distribution of traps throughout the band gap is much more complex and outside the scope of this work. It has been shown that if the distribution of traps is sufficiently narrow, the carriers will be trapped and released multiple times throughout the transit across the sample and the dispersion of carriers can be

approximated by a Gaussian function with a spread that is given in the time domain by (see, for example, [40])

$$\Delta t^2 = \frac{2\tau_r^2 L}{\tau_c \mu_o F} \qquad 3.37$$

This spread in the tail of the photocurrent is much greater than usual diffusion alone and also by space charge effects under small signal conditions [40]. It arises from multiple trapping effects.

4 Experimental Procedure

The purpose of this study was to explore the thickness dependence of electron transport in amorphous selenium layers for use in direct conversion X-ray image detectors used in mammographic screening. Eleven samples of pure selenium were deposited on indium tin oxide coated (ITO) glass by using a vacuum coater at the University of Saskatchewan. The samples ranged in thickness from 13 μm to 501 μm. Pure selenium was chosen to avoid any effects from fractionation, which occurs when there is a change in concentration of any additive near the substrate as compared to the surface of the sample.

The disadvantage of pure a-Se samples is that they tend to crystalize over time especially when exposed to light and thus are not suitable for use in commercial detectors. However the electron transport results obtained here are still helpful in understanding electron transport in stabilized a-Se.

4.1 Deposition

Vacuum deposition of selenium begins with high purity selenium pellets being evaporated inside an evacuated chamber. This selenium vapour then condenses onto the substrate held just above the glass transition temperature of a-Se to allow the selenium atoms to rearrange themselves into a structurally relaxed amorphous state as they condense. Alternative deposition techniques such as cold deposition hold the substrate well below the glass transition temperature, and in this case the atoms are essentially frozen in place as they reach the substrate.

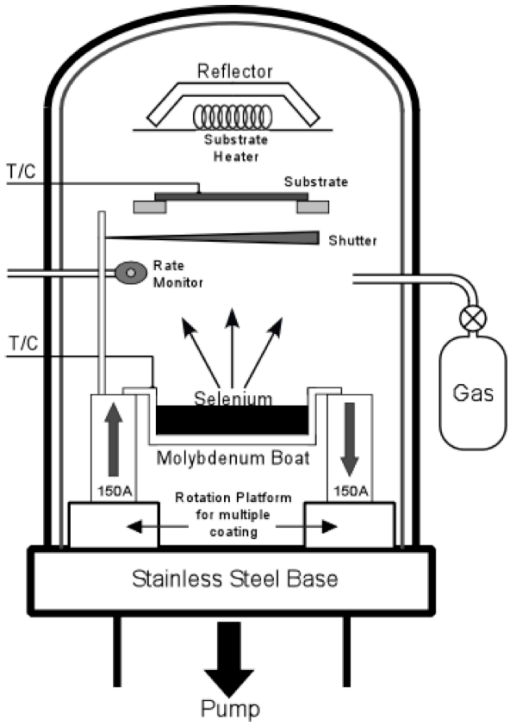

Figure 4.1 A schematic diagram of the NRC 3117 stainless steel vacuum coater used to deposit samples for this study (after Belev [8]).

As shown in Figure 4.1 the selenium pellets are held in a molybdenum boat and evaporated by running a large current through the boat. The substrate heater keeps the glass substrate around 60 °C, just above the glass transition temperature of a-Se. A mechanical shutter covers the substrate until the evaporation has reached a steady rate at which time the shutter is opened, the selenium begins to condense onto the substrate and, after the desired thickness is reached, the shutter is closed and the current switched off. The following section describes the timeline of a selenium sample deposition in more detail.

4.1.1 Deposition Procedure

First, the substrates are cleaned by submersing them in a ultrasonic bath composed of Extrain MN-01 in concentration of 2-5 g/litre of deionized water for approximately 30 minutes, changing the solution every 10 minutes. The substrates are then rinsed thoroughly in deionized water and blown off with filtered compressed air before being inserted into the substrate holder in the chamber with the conducting side facing the boat. A thermocouple is used to measure substrate

temperature during evaporation. The shutter, which is controlled by a lever outside the chamber, is positioned to cover the substrate and tested to ensure proper opening and closing as the chamber is opaque and the shutter cannot been seen during evaporation. For this study ITO coated glass was used for a substrate and two samples were deposited during each run. The larger area (50 mm × 50 mm) substrate was placed directly above the boat and a smaller (20 mm × 50 mm) substrate was placed off to the side. The effect of this was to create two different thicknesses for each run. The centre mounted sample was typically 30% thicker than the side mounted one.

Next, the boat in the vacuum chamber is charged by placing the selenium pellets in the molybdenum boat. It is important to charge the system with more selenium than will be necessary to coat the substrate since, as the boat begins to empty, the selenium evaporation can sputter, disrupting the uniformity of the sample. During the evaporation a crystal rate monitor is used to estimate the sample thickness (after adjusting for a tuning factor from previous depositions). This rate monitor needs to be checked and cleaned if necessary. The chamber is then sealed and evacuation begins.

Evacuating the chamber involves the use of two pumps. The first pumping stage uses a mechanical pump to protect the second stage diffusion pump from being exposed to atmospheric pressure. Pumping the system down to an appropriate pressure for deposition of 10^{-6} torr takes approximately seven hours.

Once suitable pressure is reached, a high current is passed through to the molybdenum boat, causing the boat to reach a temperature of ~250°C at which the selenium pellets melt and begin to vaporize. At the same time, the substrate heater warms the substrate to 60 °C, just above the glass transition temperature of a-Se. The chamber pressure, boat temperature, substrate temperature, and the evaporation rate are recorded every few minutes throughout the evaporation process.

As the boat reaches a stable temperature, the evaporation rate, as monitored by the rate monitor, will reach a constant value. At this point, the shutter is opened and the selenium deposition on the substrate begins. Once the desired thickness is reached, as estimated by using the rate monitor, and a tuning factor from previous depositions, the shutter is closed and the heaters are switched off. It is important to not run the boat dry of selenium as this creates inhomogeneities in the sample. Depositing a sample 100 μm thick will require ~50 grams of selenium pellets, much of which is lost as it condenses on the vacuum coater parts and not on the substrate.

The samples are then removed from the chamber, their thickness is checked using a micrometer at multiple locations on the surface; and they are rested in a dark chamber for at least 72 hours before top contacts are applied. The required resting period varies according to the sample composition; stabilized a-Se will require a longer resting (relaxation) period, as the structure is more rigid than that of pure a-Se.

4.2 Sputtering Contacts

To perform TOF and IFTOF experiments it is necessary to deposit an electrode or a contact on the surface of the a-Se sample. For this study, the top contacts were 0.5 cm in diameter and composed of gold. This top contact should be noninjecting to minimize dark current and be semitransparent to allow the excitation light to pass through into the sample. A Hummer VI sputtering system was used to deposit the top contact.

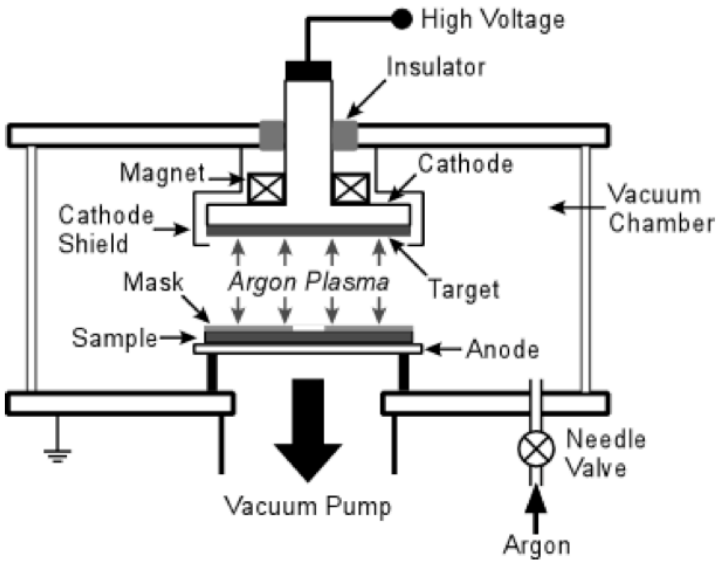

Figure 4.2 Schematic diagram of the Hummer VI sputtering system used to deposit gold contacts on the samples used in this study (after Belev [9]).

To begin the sputtering process, an aluminum mask with a circular opening 0.5 cm in diameter covers the sample. The chamber is pumped down to a pressure of 110 mTorr and filled with Argon gas. When a high voltage is applied between the anode and cathode within the chamber, the argon gas ionizes. These positively charged argon ions begin to collide with the negatively charged gold target at the top of the chamber and dislodge gold particles. These free gold particles evenly cover the exposed area on the sample surface. The sputtered gold films had an edge-to-edge resistance of between 100 Ω and 200 Ω, and were thin enough to allow light to pass through and photogenerate a sufficient number charge carriers within the sample.

4.3 Samples Deposited for this Study

For this investigation into the thickness dependence of electron transport eleven samples were deposited ranging from 13 μm to 501 μm. Samples were deposited two at a time over the course of six days at the University of Saskatchewan. All samples were rested for 72 hours after deposition before gold contacts were sputtered and measurements could begin. The twelfth ~100 μm sample crystalized almost immediately and was not available for measurements. The reason for its crystallization is not known, though it may be a rise in the substrate temperature during evaporation. The deposition times required ranged from five minutes for the

thinnest samples to four hours to deposit the 501 µm and 375 µm samples. After resting the samples, and depositing gold contacts, the thickness of each sample was measured using both a Logitech and Mitotoyo micrometer with five tests on each apparatus per sample. The thickness measurements were averaged to determine the sample thickness at the contact. Any error in the thickness measurement would have a large effect on the calculated electron mobility as the mobility depends on L^2, $\mu_e = L^2/Vt_T$, where t_T is the transit time, and V is the applied voltage. Figure 4.3 shows the thickness distribution of the samples deposited.

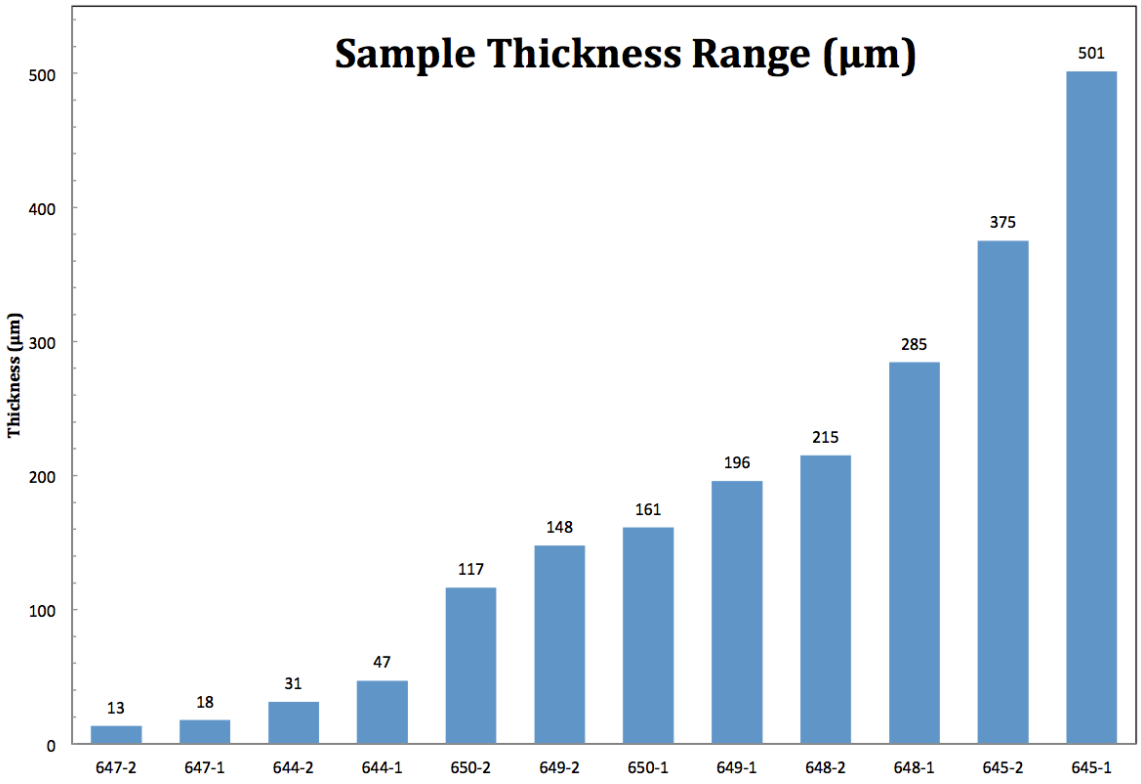

Figure 4.3 Thickness of samples deposited. Run numbers from 644 to 650 (excluding 646) with two samples per run.

The range of thickness was chosen to be as large as possible, given the limitations of TOF and IFTOF measurements. As charge transport properties vary with the applied field, it is important to test the samples at different electric fields. For the thick samples, this requires applying up to 2000 V to achieve a field of 4 V/µm, which is beyond the capability of the TOF system. Measurement of the very thin samples is limited by the speed of the external amplifier as these samples have very short

transit times, often less than 1 μs. In a typical mammographic detector the *i*-layer is ~200 μm, near the middle of this thickness range.

4.4 Charge Transport Measurements

Electron transport in each sample was measured using traditional time of flight (TOF) and interrupted field time of flight (IFTOF) techniques at various electric fields. Practical TOF and IFTOF curves observed in the case of a-Se differ from the ideal case due to the presence of localized states interacting with the charge packet as it crosses the sample. These traps can be classified as deep traps where $\tau_r \gg t_T$ or shallow traps where $\tau_r < t_T$.

In the case of carriers in deep traps they are lost from the conduction band for the length of the experiment and cease contributing to the photocurrent. If a sample contained only deep traps, the TOF response would be a delta spike at $t = 0$, followed by an exponential decay as the charge packet crosses the sample; and a sharp drop to zero at $t = t_T$ as the only dispersion would be due to mutual columbic repulsion, and carrier diffusion. These deep traps control the free carrier lifetime in the sample.

A carrier trapped in a shallow trap is most likely to be released back into the conduction band within the timeframe of the experiment. This release relies on interaction with phonons in the lattice structure and therefore shows a temperature dependence, as these interactions are more frequent at higher temperatures. Due to multiple trapping and release events, shallow traps limit the carrier mobility and lead to charge packet dispersion as some carriers are held for longer, and some shorter periods. Consequently, the carriers do not all arrive at the same time at the rear electrode but arrive with a distribution of transit times.

Spear [28], Kepler [42], Leblanc [43], and Brown [44] first pioneered the TOF technique while studying charge transport in high resistivity solids. Since then the technique has become an invaluable tool for measuring charge transport in a wide

range of highly resistive materials, including organics. The following section details a TOF and IFTOF system used in this study.

4.4.1 Determining Carrier Mobility from TOF Experiments

Once the TOF experiment has been performed, the waveform must be analyzed to find the carrier mobility. For this procedure, it is assumed that the carriers are generated very close to the semi transparent gold electrode within the absorption depth δ. This means that the electrons will cross the entire length of the sample L, while the holes will be absorbed by the negatively biased top contact almost immediately. The average electron drift velocity (assuming the top electrode is negative) is calculated as,

$$v_d = \frac{L}{t_T} \qquad 4.1$$

As described in this section, the internal field is assumed to be constant $F = V/L$ so that the drift mobility can be found by,

$$\mu_e = \frac{v_d}{F} = \frac{L^2}{V t_T} \qquad 4.2$$

where μ_e is the electron drift mobility, F is the applied electric field (V/μm), L is the sample thickness V is the applied voltage, and t_T is the transit time.

4.4.2 Definition of t_T

The determination of the electron mobility using Equation 4.2 involves a simple calculation, however difficulty arises when defining and measuring the transit time. The chosen definition of transit time can have a significant effect on the calculated mobility, which makes comparison between different data sets difficult.

When observing a practical TOF waveform taken on an a-Se film, three transit times can be defined as shown in Figure 4.4. The shortest corresponds to the knee of the

curve when the first carriers reach the bottom contact and exit the sample. Another practical definition is the half current point when half of the carriers have reached the bottom electrode as indicated in Figure 4.4. Yet another possible transit time definition is based on taking the inflection point that corresponds to the peak of the charge carrier packet that reaches the rear electrode. These three points are illustrated in Figure 4.4.

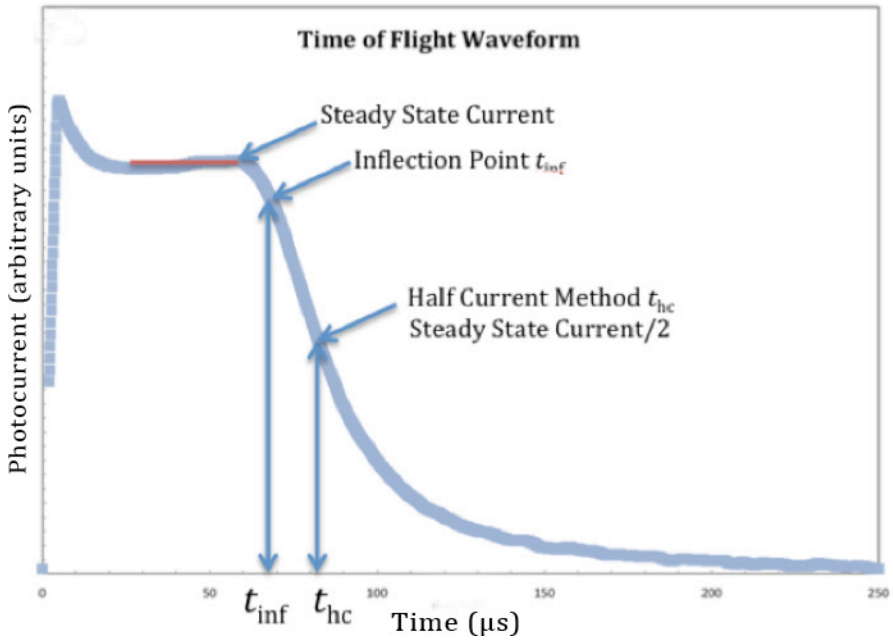

Figure 4.4 Three different points on the TOF curve can be used to define the transit time causing a large change in the calculated mobility. Note that on an ideal TOF curve all three of these points would occur at the same time as the current drops to zero immediately.

In Figure 4.4, the difference in calculated mobility was 28% between the half current method and knee method. In highly dispersive charge carrier transport, the photocurrent tail can extend for almost as long as the steady state current before reaching 10% of the steady state current value. In these samples, the difference between the three definitions of transit time becomes even greater.

Finding the knee and half current points on the TOF curve is straightforward, and need to be described in detail. However, the photocurrent tail inflection point is determined by differentiating the photocurrent waveform numerically. The peak of

the derivative occurs when the peak of the drifting carrier distribution reaches the bottom contact, which indicating the inflection point.

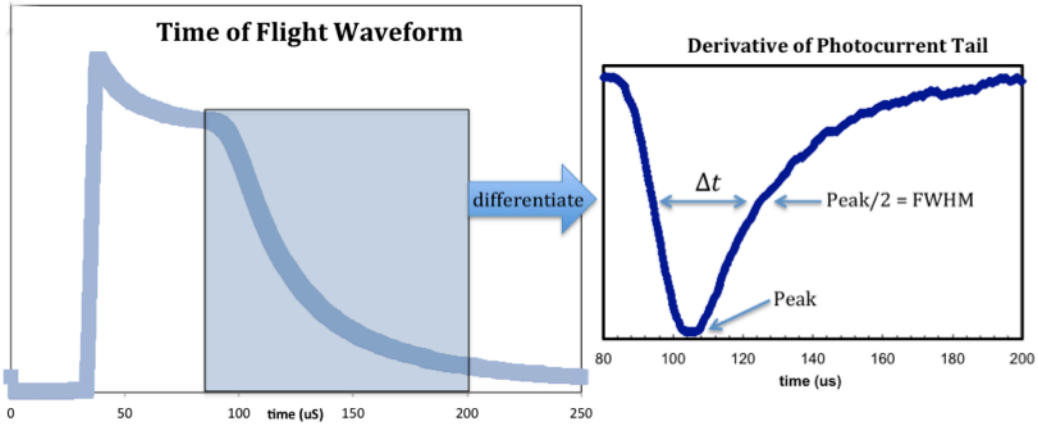

Figure 4.5 Differentiating the tail of the photocurrent curve numerically shows the inflection point.

As shown in Figure 4.5, this process also yields the charge packet dispersion, calculated at the full width half maximum; the dispersion of different samples is investigated in Section 5.6.

4.4.3 Determining Carrier Lifetime from IFTOF Experiments

While TOF experiments are useful for determining carrier mobility in a-Se, interrupted field time of flight (IFTOF) experiments are used to calculate the carrier deep trapping lifetime. If the deep traps are assumed to be at one energy level within the band gap (one τ_c for deep traps) the fractional recovered photocurrent after interruption is related to the interruption time by,

$$\frac{v(t_2)}{v(t_1)} = \exp\left(-\frac{t_i}{\tau_e}\right) \qquad 4.3$$

where τ_e is the effective electron lifetime. When the IFTOF experiment is performed multiple times, with varying interruption time, the results can be tabulated and plotted on a semi logarithmic plot and the slope of the best fit line yields the carrier deep trapping lifetime as shown in Figure 3.7.

It is important to note that an IFTOF experiment yields the carrier lifetime with zero applied field (during interruption) at one position within the sample ($l = \mu V t_1/L$). This means that IFTOF experiments can be used to measure inhomogeneities in non pure a-Se samples as the delay time (t_1) can be changed to stop the carriers at different locations throughout the sample. It should be noted that at very long interruption times, the carriers will disperse significantly due to their mutual coulombic repulsion; and if the interruption is near one of the contacts, some of the carriers may exit the sample during the interruption.

Building a system for IFTOF measurements adds significant complexity to a conventional TOF system due to the requirement of switching a large voltage bias as the carriers cross the sample. Without techniques to eliminate the switching transients, the photocurrent signal would be lost as it is orders of magnitude smaller than the applied bias.

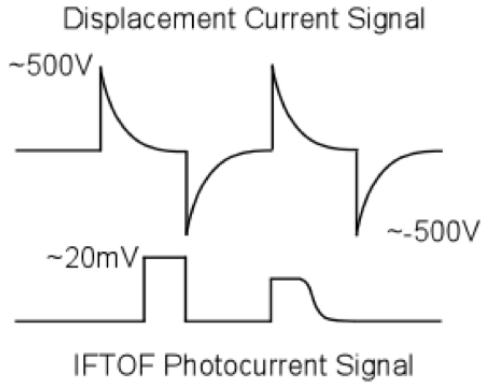

Figure 4.6 Without removing the switching transients during a IFTOF experiment the photocurrent signal would be lost. Typical applied biases range from 1-4 V/μm (10-1000 V) and typical photocurrent signals are in the mV range (after Fogal [2]).

The displacement current signal decay shown in Figure 4.6 is due to the combined *RC* constant of the sample and sampling resistor connected in series, as shown in Figure 4.7.

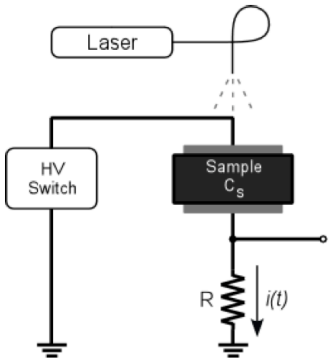

Figure 4.7 The RC constant of the sample capacitance and sampling resistor cause a transient decay in the switching voltage (after Fogal [2]).

To eliminate this transient voltage, the experiment is performed twice; first without photo excitation to record the displacement current signal and then with photo excitation and the two signals are subtracted leaving just the photocurrent signal.

4.5 TOF and IFTOF Experimental Setup

This section details each part of the TOF and IFTOF experimental system used in this study that is suitable for studying a-Se layers. The requirements of such a system include:

1) A short duration light pulse in the blue or ultra violet range that can be channeled through a fiber optic cable to illuminate the sample, the laser used in this study was a LN103C nitrogen pumped laser with peak output at 337.1 nm, and 0.1 nm spectral spread.
2) A high voltage switch capable of switching up to 1000 V (2 V/μm for the thickest sample). For IFTOF experiments, the switching transients must be eliminated or the photocurrent signal will be lost.
3) A sample holder with low impedance contacts to apply the electric field across the sample.
4) A sampling resistor that can be changed to accommodate varying photocurrent magnitudes. This resistor converts the I-mode photocurrent signal to a voltage signal The output signal $v(t) = i_{\mathrm{ph}}(t)R$ can be increased by increasing *R* at the expense of a larger *RC* time constant, which is the combination of the sampling resistor, the sample capacitance, and any stray

capacitance from cables and connections. For useful measurements, R should be selected so that $RC \ll t_T$.

5) A fast (large bandwidth) amplifier to amplify the signal across the sampling resistor for display on an oscilloscope.
6) A trigger generator controlled by a computer to control the HV switch, laser pulse, amplifier protection, and oscilloscope.
7) A computer to capture and analyze TOF and IFTOF signals, as well as control the triggering circuitry.
8) For IFTOF experiments, a method to eliminate the displacement current without damaging the amplifier. This study used a grounded bridge network with a variable capacitor (C_{NS}) in parallel with the sample, which can be tuned to match the sample capacitance.

Figure 4.8 shows an overview of the system meeting these requirements that was used in this study. The rest of Section 4.5 describes this system in detail. Researchers at the University of Saskatchewan previously developed the TOF system used for this study.

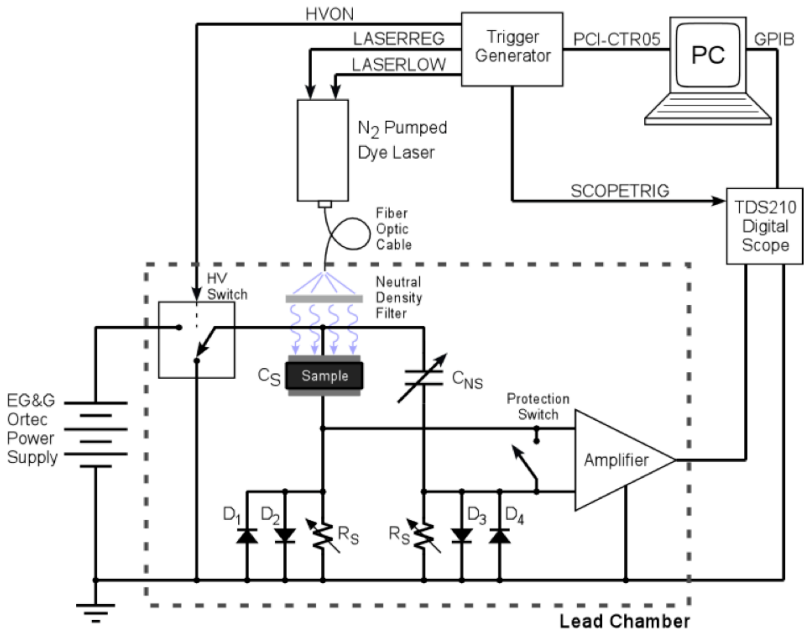

Figure 4.8 Schematic overview for the TOF and IFTOF capable system used in this study.

4.5.1 Amplifier

A two stage wide band differential amplifier is used to amplify the induced photocurrent signal across the sampling resistor. The first stage uses an Analog Devices AD830 wide bandwidth, high CMMR video amplifier. This stage is configured to amplify the differential photocurrent signal from the displacement current signal. The second stage uses an Analog Devices AD827 non-inverting operational amplifier configured with 16 dB of gain to raise the signal above the noise floor of the oscilloscope and to drive the capacitance of the coaxial line connecting the amplifier to the oscilloscope.

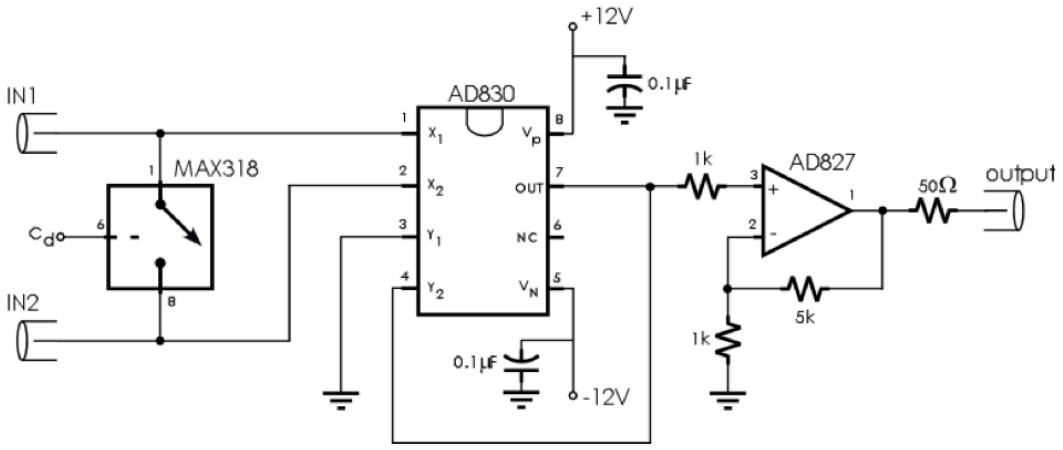

Figure 4.9 A two stage differential amplifier with 16 dB of gain used to amplify the photocurrent signal for display on an oscilloscope. The two inputs are connected to either side of the bridge network shown in Figure 4.8, the output is a coaxial cable connected to an oscilloscope.

To protect the amplifier from the high voltage switching transients a Maxim MAX318 normally open single pole single throw switch is connected across the inputs of the differential amplifier.

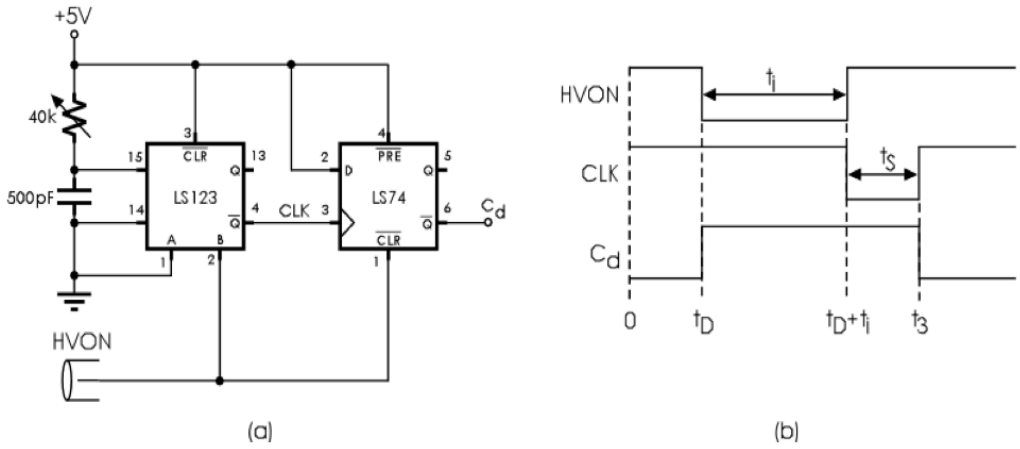

Figure 4.10 Schematic (a) and timing diagram (b) for the amplifier protection stage.

As shown in Figure 4.10, the protection logic uses a monostable multivibrator (LS123) and a D flip-flop to trigger the switch. The trigger pulse delay after the high voltage is switched on can be varied with the 40 kΩ potentiometer. Estimating the amplifier bandwidth by measuring the response to a 100 mV, 130 ns pulse shows a bandwidth of ~12 MHz, this is sufficiently wide to measure the thinnest samples in the study where the shortest transit time will be in the µs range.

4.5.2 HV Switch

To properly compare samples with different thicknesses, the same electric field should be applied. For this work the applied electric field ranged from 1 - 4 V/µm translating to a high voltage switch capable of switching between 10 V and 2000 V. The setup used in this case was limited to 1000 V, which limits the thickest sample measurements to 2 V/µm. However, this still allowed most comparisons to be performed. The HV switch uses two fast switching *n*-channel HEXFETS in a totem pole configuration.

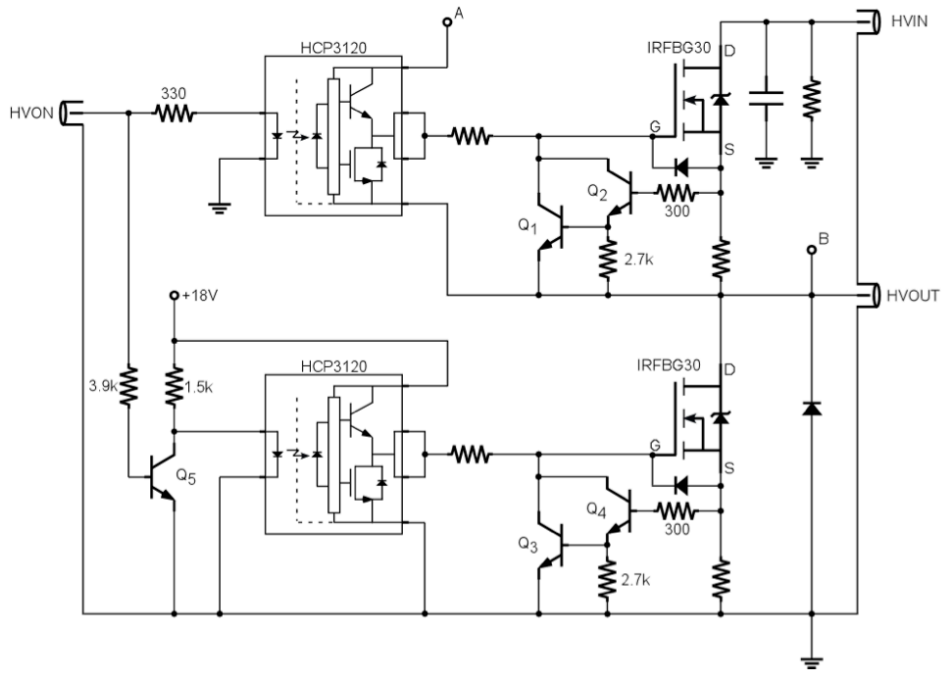

Figure 4.11 Schematic of a HV switch capable of switching up to 1000V. The inputs are HVON, connected to the trigger generator, and HVIN connected to a high voltage supply. The output HVOUT is connected to HVIN when HVON is triggered.

The HEXFETs are shown in Figure 4.11 as HCP3120 with their power coming from a floating 18 V supply. The BJT transistors (Q1 - Q4) provide protection to the HEXFETS in case of a fault on the output since if the output current exceeds its maximum rating, Q1 and Q3 will switch on providing a short circuit path between the gate and source terminals.

4.5.3 Laser

All TOF and IFTOF experiments require a short duration high intensity light pulse to photogenerate charges just inside the sample. Though a Xenon flash can be used as in various other TOF and IFTOF systems, the ideal light source is a pulsed laser, due to the short duration of pulses that can be generated. The experiments performed in this study used a nitrogen pumped LN103C laser with pulse duration of ~300 ps, ±2 ns jitter, power of 250 kW, and a peak spectral output at 337.1 nm (UV) with a 0.1 nm spread. This laser pulse is then fed through a Newport Optical Fiber adapter and into the lead chamber where the samples are placed for testing. It is possible to add a neutral density filter to reduce the number of photons within the laser path if the output is too intense, and the small signal condition is not satisfied. The output of

the fibre optic cable is placed approximately 10 cm above the top contact of the sample and a black mask slightly smaller than the contact diameter is placed over the semitransparent top contact to stop any edge illumination and fringing effects.

The LN103C laser uses TTL signals to initiate triggering. Two signals must be applied to the inputs within 50 μs or the laser will self fire to discharge.

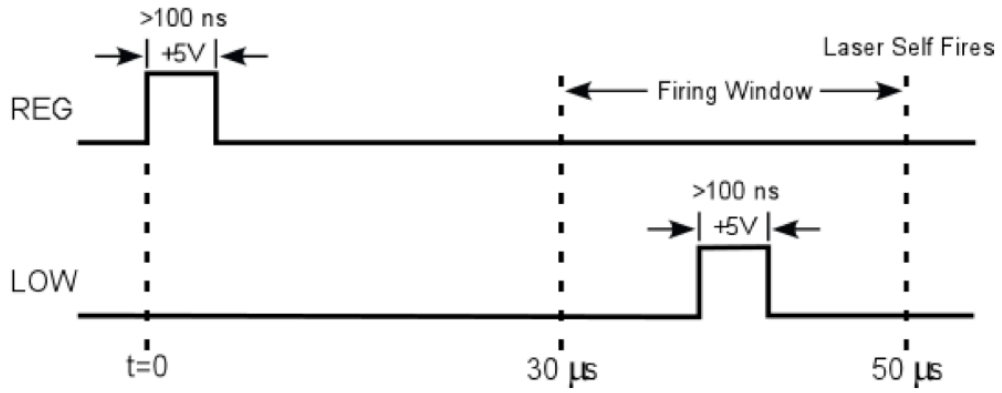

Figure 4.12 Timing diagram for proper triggering of the LN103C laser using TTL signals.

Two inputs (REG and LOW) with BNC connections are used to fire the laser by creating a high voltage discharge across a spark gap. The timing begins with a pulse (with width longer than 100 ns) applied to REG. Between 30 - 50 μs later, a second 100 ns pulse must be applied to the LOW input or after 50 μs the laser will self fire. These inputs have been coupled to the rest of the circuitry optically to avoid the feedback from large voltage switching transients effecting measurements.

4.5.4 Trigger Generator

To capture a TOF or IFTOF signal, a trigger generator circuit is required to ensure all the sections of the circuit are activated with the proper timing. The trigger circuit is an AMD 9513 counter board containing five 16 bit up-down counters which is connected to a PC; and is programmable using C++.

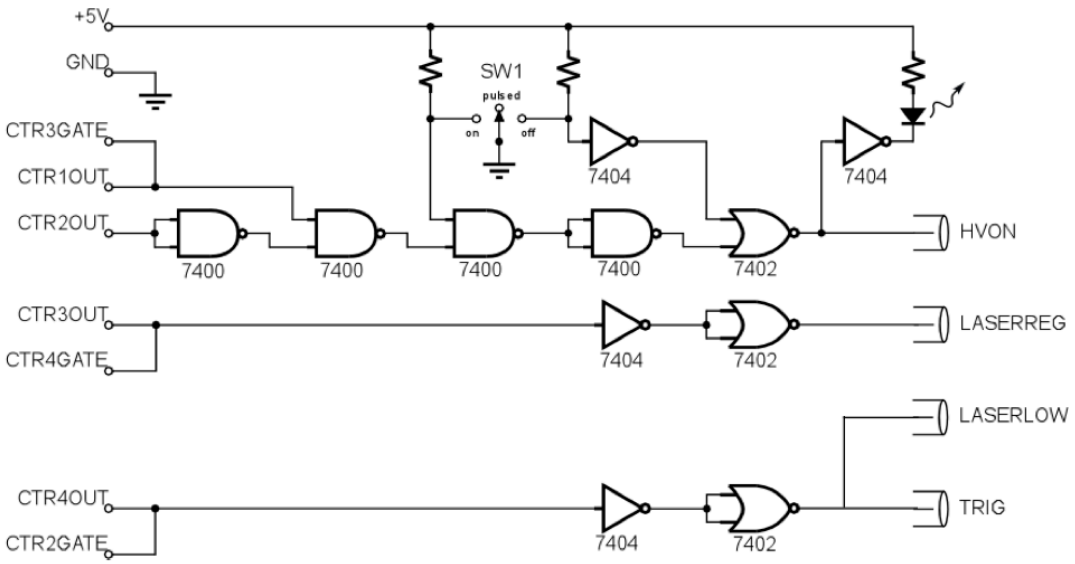

Figure 4.13 Trigger generator logic showing the four outputs; HVON, LASERREG, LASERLOW, and TRIG. One switch is included to allow manually setting the HV to; always on, always off, or HV control by this circuit.

A timing diagram for a IFTOF experiment is shown in Figure 4.13 with an interruption time t_i.

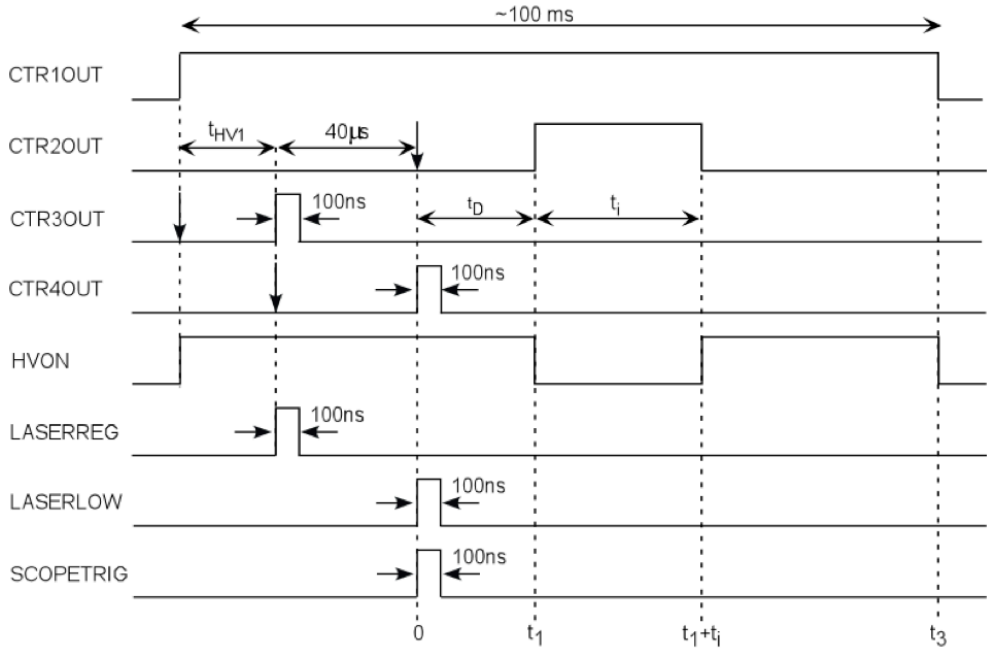

Figure 4.14 Timing diagram for an IFTOF experiment.

As shown in 4.14 the LASERLOW and TRIG outputs are triggered at the same time. This allows the oscilloscope to be protected from the high voltage transients but still capture and display the photocurrent as the charge is photogenerated by the laser.

4.5.5 Signal Capture

The photocurrent signal is captured on a Tektronix TDS210 oscilloscope with a sampling rate of 1 GS/s. This oscilloscope is connected to a personal computer to allow the photocurrent traces to be saved for further analysis, comparison and archiving.

To limit the noise at the input of the oscilloscope, the bandwidth was limited to 20 MHz, which is still much wider than minimum bandwidth required to properly capture the photocurrent signal. Custom software on the PC has been developed to control the trigger circuit. This software also performs the double excitation routine required for IFTOF measurements, energizing the bridge without excitation, capturing that signal, then energizing the bridge again with photoexcitation and subtracting the two signals to determine the true photocurrent, while eliminating the displacement current, provided the bridge is properly balanced.

4.6 Summary

As detailed in Section 4, eleven samples of pure a-Se were deposited with thicknesses ranging from 13 μm to 501 μm. Conventional vacuum deposition was used to fabricate the a-Se layers on ITO glass substrates. The films were all deposited at a substrate temperature of 60 °C, which is above the glass transition temperature. Conventional time of flight and interrupted field time of flight measurements with applied fields of 1, 2, and 4 V/μm (except for the 501 μm and 375 μm sample due to the 1000 V limitation) were performed on each sample to determine the electron mobility and lifetime. These photocurrent waveforms were saved for later analysis, including an investigation into the effect of the definition of transit time on the calculated electron mobility, and carrier dispersion at different fields. The results are presented in Section 5.

5 Results and Discussion

5.1 Introduction

This section presents the results of this study including the thickness dependence of electron transport in a-Se, carrier range and Schubweg, effect of the definition of transit time, and charge packet dispersion. All the measurements presented in this section were performed multiple times to ensure accuracy.

5.2 Measuring Charge Transport

Two of the parameters of interest in the description of charge transport in the case of a-Se based photoconductors: carrier drift mobility (μ) and carrier deep trapping lifetime (τ). Conventional time of flight (TOF) experiments can be used to determine mobility μ, and interrupted field time of flight (IFTOF) measurements can be used to determine the carrier lifetime τ.

5.2.1 Conventional TOF Experiments to Determine Carrier Mobility

Assuming the small signal condition, where the electric field is constant throughout the sample, mobility can be calculated from a TOF waveform as shown in Figure 5.1 [45].

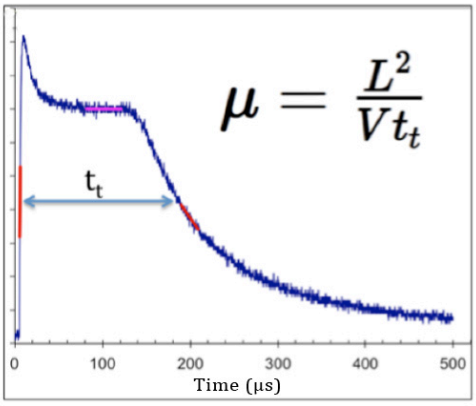

Figure 5.1 TOF waveform showing a possible definition of a transit time and calculation of the corresponding drift mobility.

Note that in the mobility calculation, V is the total applied voltage (i.e., 100 V) but for charge transport comparisons between samples, it is important to compare measurements at the same field, as it has been shown that the mobility increases with increasing electric field in a-Se.

In this work, the high voltage bias was applied a few milliseconds before firing the laser to ensure the internal field was stable when the carriers were photoinjected into the sample.

5.2.2 IFTOF Experiments to Determine Carrier Lifetime

To calculate the electron lifetime in a-Se, multiple IFTOF experiments were conducted varying the interruption time t_i but keeping the applied field and delay time constant. The fractional recovered photocurrent (i_2/i_1) can then be determined by comparing photocurrent immediately before and after interruption as shown in Figure 5.2.

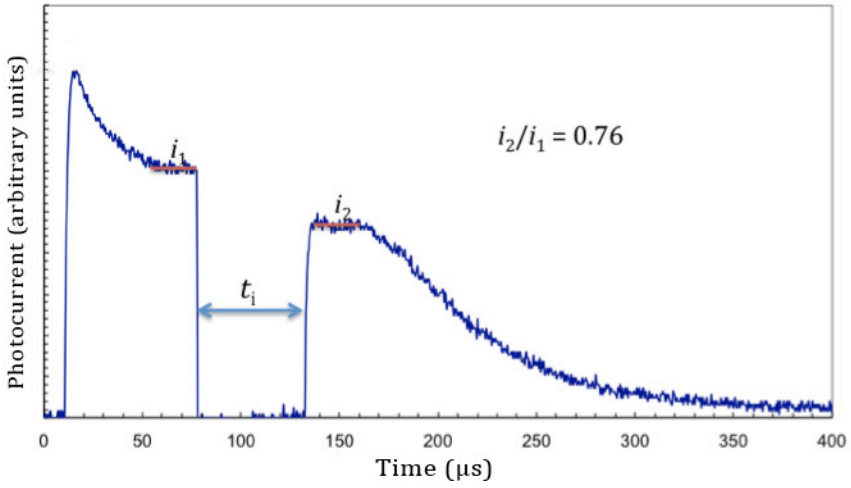

Figure 5.2 Determining the fractional recovered photocurrent (i_2/i_1) in a IFTOF signal where the displacement current has been completely removed by the double bridge excitation method described in Section 4.

As the interruption time becomes longer, i_2/i_1 will become smaller as more carriers are trapped in deep traps during the interruption period. Lifetime measurements reported here were performed at an applied field of 2 V/μm, and the interruption

time ranged from $t_i \sim 0.1 t_T$ to as long interruptions times as possible before $\frac{i_2}{i_1} < 0.1$, that is, when less than ten percent of the carriers are recovered upon the reapplication of the bias. These results are plotted on a semi logarithmic plot shown in Figure 5.3.

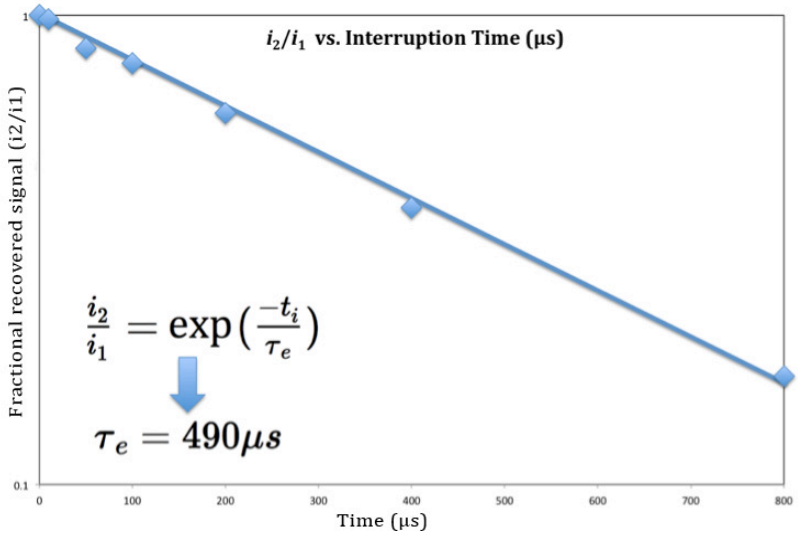

Figure 5.3 Plotting the fractional recovered photocurrent vs. interruption time on a semi logarithmic plot yields the electron lifetime from the slope of the best fit line. In this case i_2/i_1 ranged from 0.2 to 0.9 and the deep trapping lifetime, from the slope of the line, τ_e was 490 μs.

5.3 Thickness Dependence of Electron Transport in a-Se

5.3.1 Background

It has been well established that electron mobility increases with increasing applied electric field. This result is also observed in this study. If one uses the discrete binary trap distribution model of charge transport described in Section 3.4.2, where shallow traps located around 0.3 eV below the conduction band, with corresponding release time $\tau_{r1} \sim 0.1 - 1$ μs, control the electron mobility, and deep traps located around 1.05 eV below the conduction band with release time much greater than the transit time $\tau_{r2} \gg t_T$ control electron lifetime, it is not expected that electron transport would show a strong thickness dependence. However the results of this study do not support this assumption.

5.3.2 Drift Mobility

Figure 5.4 shows the measured electron drift mobility at a field of 2 V/μm in eleven pure a-Se samples with thicknesses between 13 μm and 501 μm. The definition of the transit time t_T for μ calculations is shown in Figure 5.1

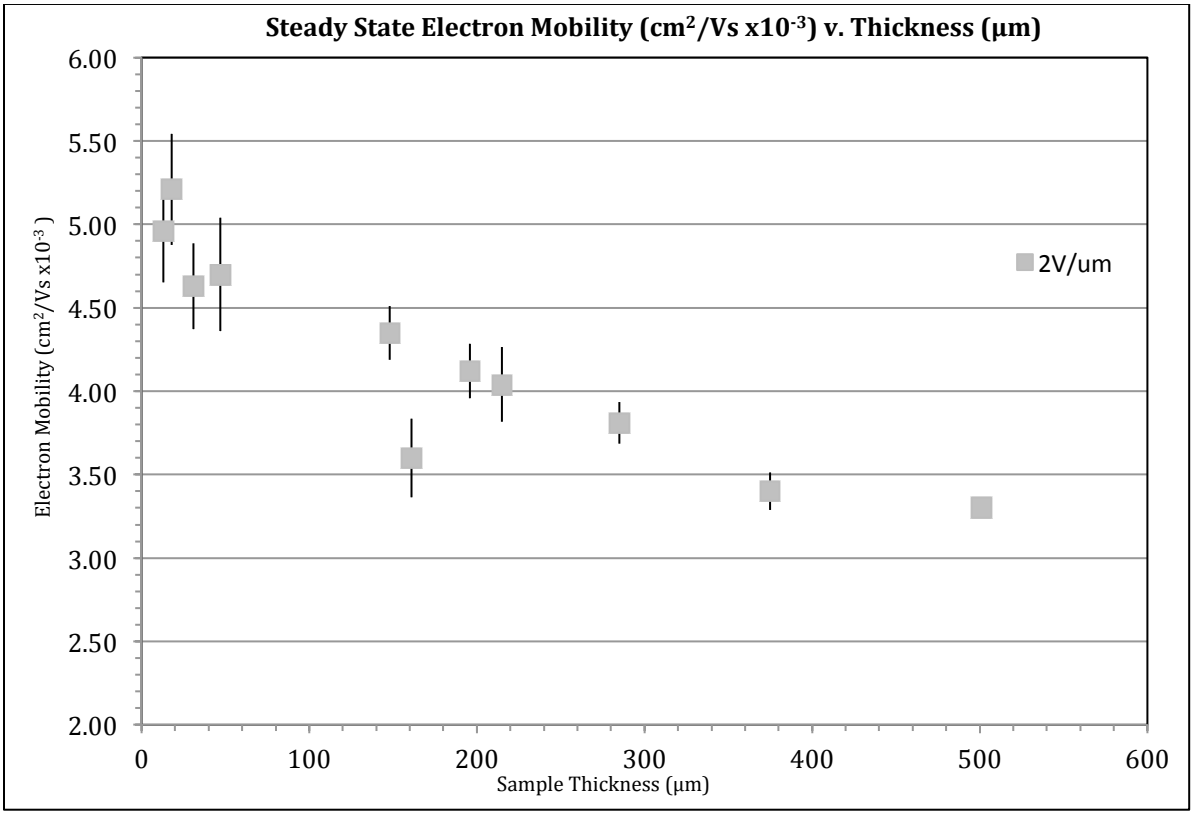

Figure 5.4 Electron mobility at 2V/μm showing an inverse relationship between mobility and sample thickness.

Electron mobility ranged from 3.30×10^{-3} cm^2/Vs to5.21×10^{-3} cm^2/Vs, well within the expected range for electron mobility measurements reported on pure a-Se. The error bars shown in Figure 5.4 are due to uncertainty in the measured thickness of the samples, which ranged from 1% to 10%, which leads to an error in the drift mobility determination.

The TOF experiments for the measurement of drift mobility were performed at three electric fields corresponding to 1, 2 and 4 V/μm. These results are shown in Figure 5.5 as drift mobility vs. thickness plots for the three different electric fields.

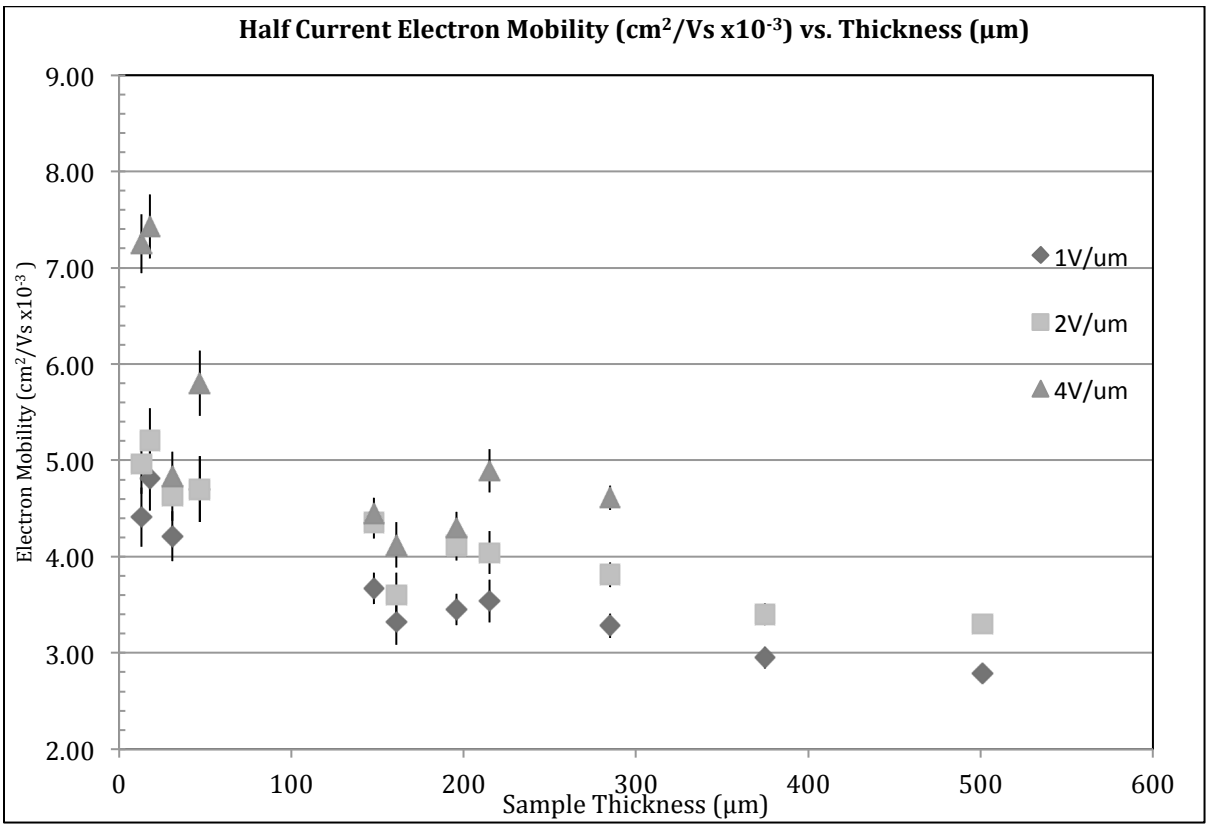

Figure 5.5 Comparison of electron mobility vs. thickness at different applied fields.

As expected the electron mobility increases as the applied field is increased [8], this characteristic was more noticeable in the thinner samples where, for the 13 µm sample, the mobility increased from 4.41×10^{-3} cm^2/Vs at 1 V/µm to 7.25×10^{-3} cm^2/Vs at 4 V/µm; a significant increase.

5.3.3 Lifetime or Deep Trapping Time

The determination of the carrier lifetime involves examining the ratio i_2/i_1, which indicates the fraction of carriers being trapped during the interruption time t_i in the absence of an applied field. There is, of course, a small internal field due to the space charge of the photoinjected carriers. For each sample, the electron lifetime was measured at an applied field of 2 V/µm.

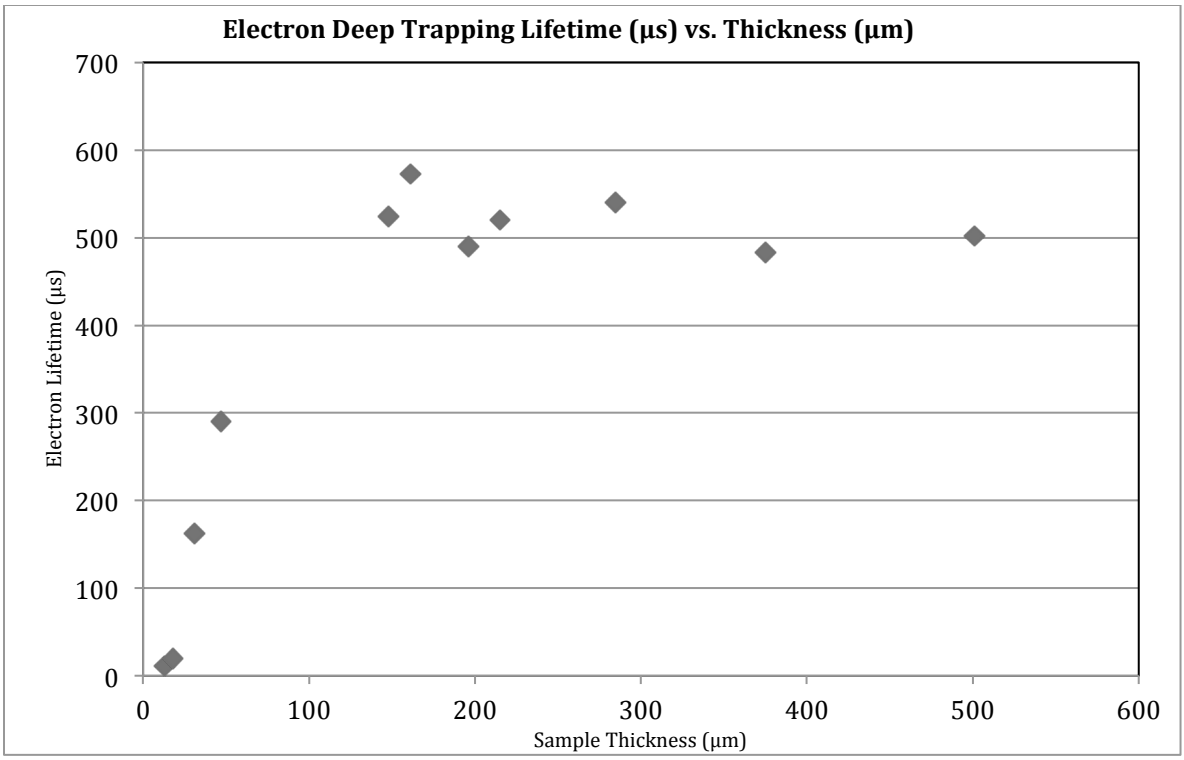

Figure 5.6 Electron lifetime vs. thickness as measured at 2 V/μm.

Figure 5.6 shows that electron lifetime is relatively consistent in the samples of thickness greater than ~150 μm , but drops off quickly in samples thinner than 50 μm. These observations differ significantly from the result suggested by the binary trap distribution mode for charge transport, as the deep trapping lifetime should not change with thickness provided that we can assign a shallow and deep sets of traps to describe charge transport.

This sharp drop in electron lifetime combined with the inverse relationship between mobility and thickness suggests the existence of a third intermediate trap level, which acts as a shallow trap in thick samples with long transit times but as a deep trapping level in thinner samples. Put differently, the third level as a release time such that it is shorter than typical transit times in thick samples, and hence it acts as a quasi-shallow trap in these samples. On the other hand, in thin samples, the release time is longer than typical transit times.

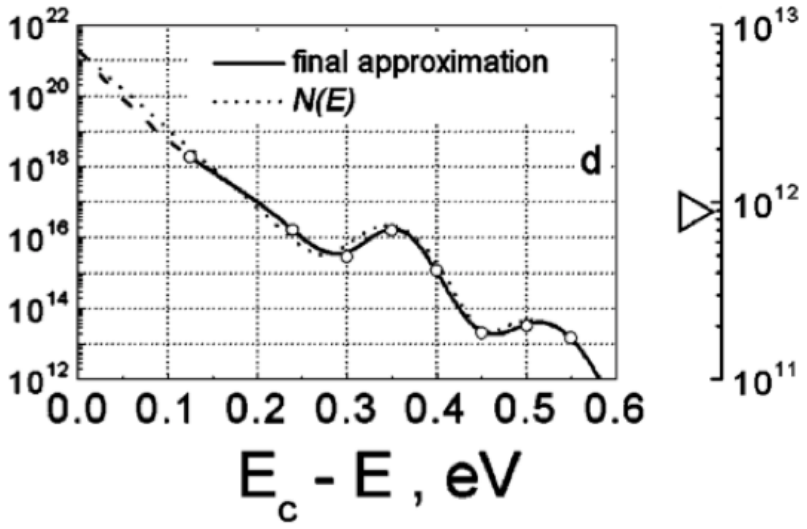

Figure 5.7 A proposed density of states model near the conduction band for a-Se (after Koughia et al. [46]).

Figure 5.7 shows the density of states (DOS) model proposed by Koughia et al. [46] in which the authors compared measured and calculated TOF curves to find a plausible DOS distribution. According to the latter work, the third intermediate trapping level may be located at around 0.45 – 0.55 eV below $E_{c,}$ corresponding to a release time of $\tau_{r3} \sim 30 - 300$ μs and a trap concentration around 10^{-13} $\mathrm{eV}^{-1}\mathrm{cm}^{-3}$. On the other hand, the shallow trap level is located around 0.30 eV below the conduction band edge with a large concentration of $\sim 10^{16}$ $\mathrm{eV}^{-1}\mathrm{cm}^{-3}$; the corresponding release time $\tau_{r1} \sim 0.1 - 1$ μs. If we compare τ_{r3} and τ_{r1} with the transit time in a 13 μm sample, where $t_T = 1.6$ μs, and it is evident that the carriers trapped in the intermediate trap level will not have time within the duration of the experiment to be released back into the conduction band, therefor these traps act as a deep trapping level in these thin samples. On the other hand those traps with $\tau_{r1} \sim 0.1 - 1$ μs will continue to act as shallow traps even in this thin sample.

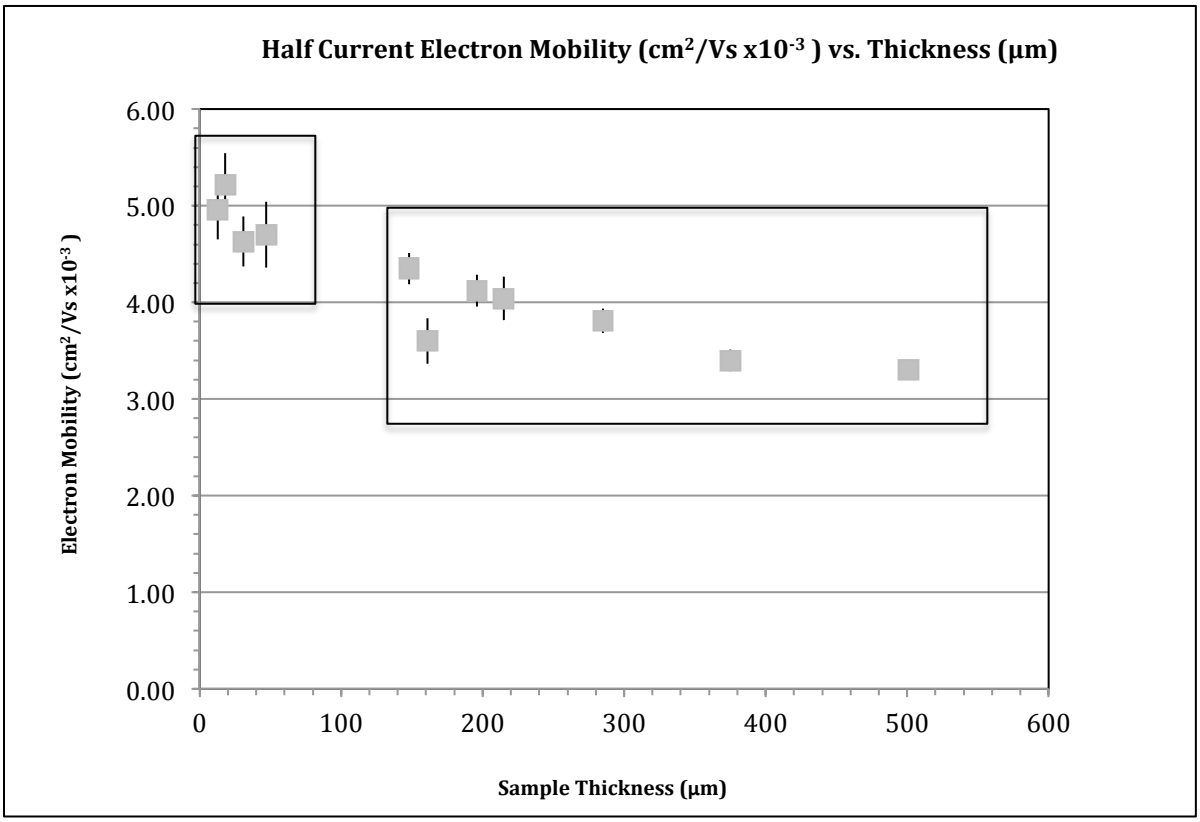

Figure 5.8 Classifying the a-Se samples as either thin samples where $0 < t_T < \tau_{r3}$ which occurs in samples thinner than 50 µm and thick samples where $t_T < \tau_{r3}$ allowing for carriers to be released within the transit time.

Given the sharp drop in the electron lifetime in thin samples it is useful to reconsider the drift mobility vs. thickness findings. Figure 5.8 clearly identifies the separation in mobility values between the thin samples (less than 50 µm) and thicker samples (150 µm and greater). This classification can also be applied to the lifetime measurements as illustrated in Figure 5.9.

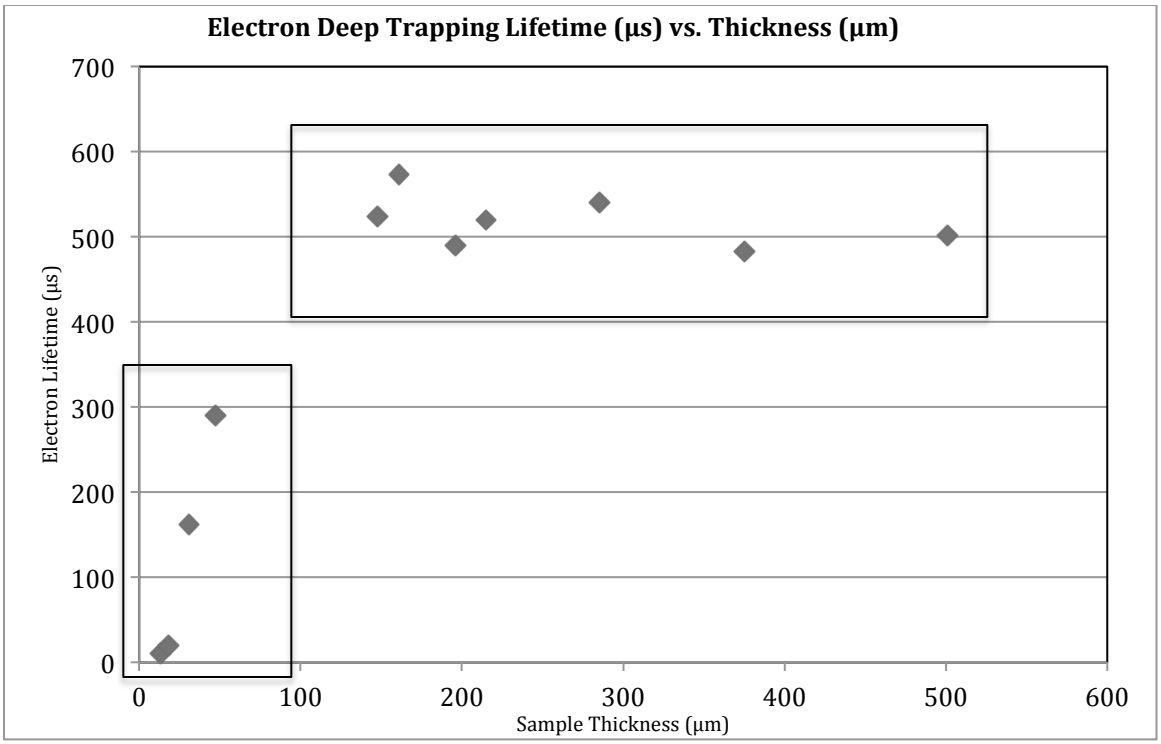

Figure 5.9 In thin a-Se samples the intermediate trap level drastically reduces carrier lifetime.

The following table describes the different trap levels present in a-Se, their relative concentrations, and their classification as either shallow or deep trap levels based on TOF and IFTOF experiments and the DOS model proposed by Koughia et al.

Location (eV below conduction band)	**Concentration ($eV^{-1}cm^{-3}$)**	**Classification**
~0.3	$\sim 10^{16}$	Shallow traps
0.45 - 0.55	$\sim 10^{13}$	Intermediate level traps
< 0.70	$\sim 10^{12}$	Deep traps

Table 5.1 Classification of trapping levels from TOF and IFTOF experiments.

5.4 Carrier Range and Schubweg

Two parameters of interest for detector design are the average carrier range ($\mu\tau$), which is the average distance a carrier will travel per unit field before being trapped, and the carrier Schubweg, which is the average distance a carrier drifts before being trapped, and includes the applied field ($\mu\tau F$). These two parameters

are important since the choice for the photoconductor layer thickness must be struck between absorbing the most of the incident radiation as possible (thicker layer) and allowing the generated charge to reach the collecting pixel electrodes to form an image (thinner layer).

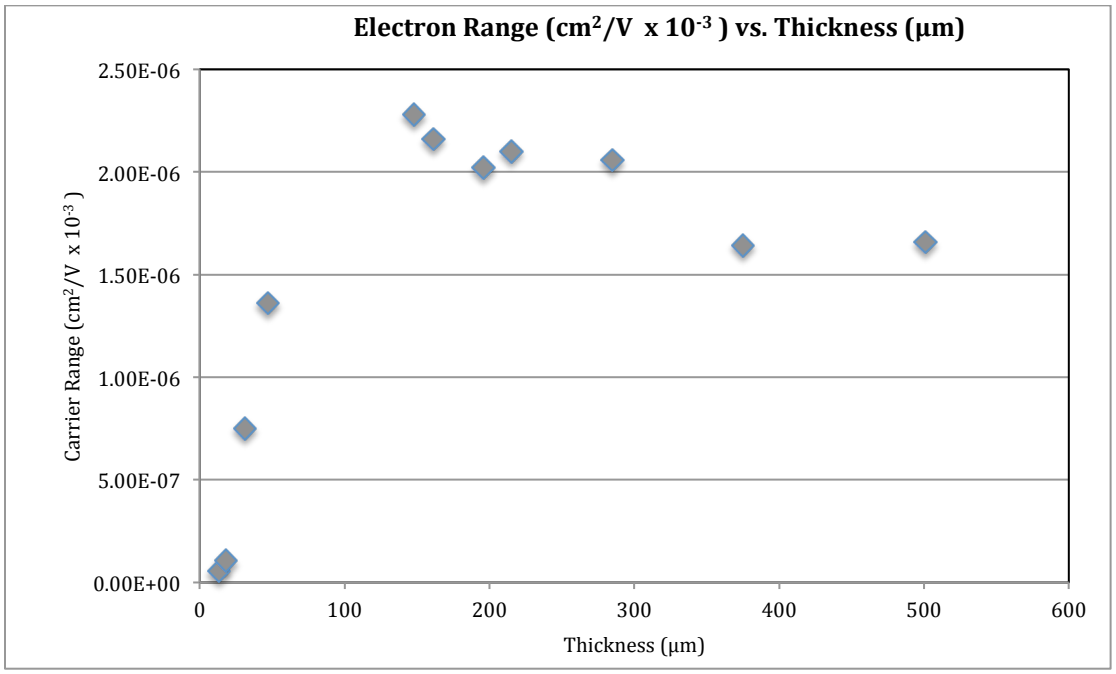

Figure 5.10 Electron range in samples ranging from 13 µm to 501 µm.

As the electron lifetime in the thin samples was so drastically reduced the carrier range in these thin samples is much shorter than those in thick samples as illustrated in Figure 5.10. Basically, the large drop in the carrier lifetime dominates the fall in the carrier range as the sample becomes thinner. The electron range was 5.46 x 10^{-8} cm^2/V in the 13 µm sample as opposed to 2.28 x 10^{-6} cm^2/V in the 148 µm sample, that is, the electron range in the 13 µm sample is only 2.3% that in the 148 µm samples.

5.5 Effect of Definition of Transit Time

5.5.1 Background

As mentioned in Section 4.4.2, the charge carrier transit time from TOF curve can be defined in three different ways based on the operational definition of transit time, as shown in Figure 4.4 and 5.11 the three methods are: (i) the half current method which defines the transit time as the time when half the carriers present in the steady state current have reached the collecting electrode; (ii) the inflection point method, which defines the point at which the peak of the charge carrier distribution reaches the collecting electrode; (iii) the knee of the TOF curve where the first or the fastest carriers reach the electrode. The dispersion of the drifting charge carrier packet during its drift across the sample, and also the shape of the carrier packet as it reaches the rear electrode, affect the differences between these operational definitions of the transit time and correspondingly the calculated drift mobility.

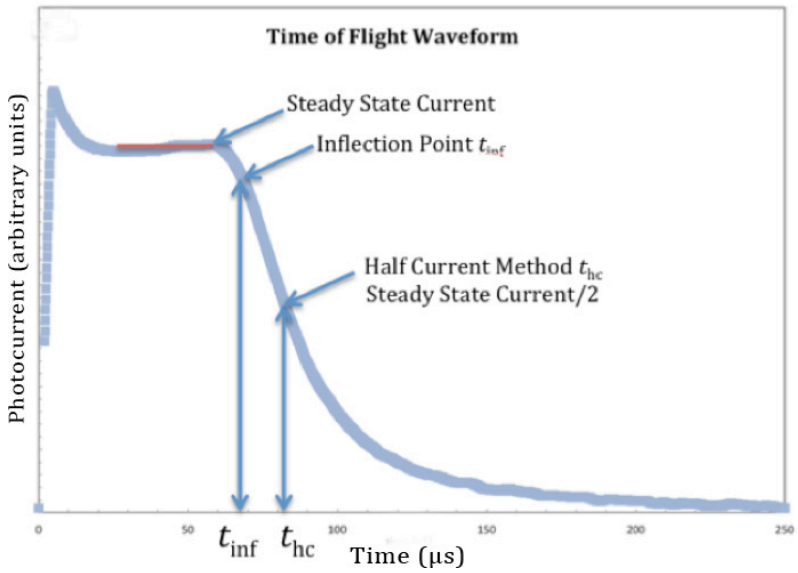

Figure 5.11 The inflection point and half current point suggest two different transit times on the sample TOF current waveform.

5.5.2 Variations in the Drift Mobility

This study does not include the knee method as this was primarily used when TOF techniques were first being developed as waveforms could not be saved to a computer and the knee of the curve was the only feasible point that could be

measured. The variation in the drift mobility as determined from the inflection point method and half current method ranged from ~1% to ~24% where samples with more dispersion showed a larger difference between the two methods. Figure 5.12 compares the drift mobility calculated from these two methods as a function of sample thickness. Notice that both mobilities show the same trend as a function of sample thickness; thinner samples exhibit greater electron drift mobilities.

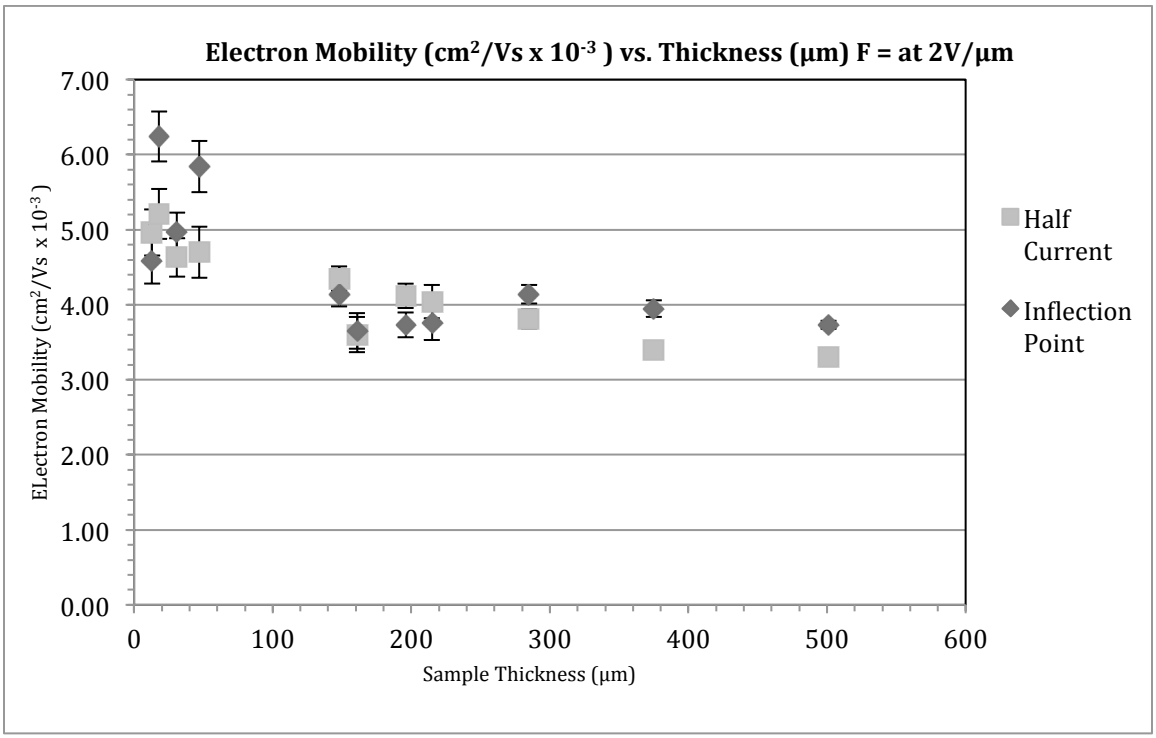

Figure 5.12 Comparison of half current and inflection point methods when calculating electron mobility from TOF waveforms.

5.6 Pulse Dispersion

5.6.1 Background

The short duration light pulse provided by the nitrogen pumped laser creates a near uniform sheet of charge just inside the a-Se layer beneath the top contact. However as the charge packet drifts and crosses the sample under the influence of the applied field, it is dispersed due to various mechanisms: (a) mutual coulombic repulsion between carriers of the same charge, (b) carrier diffusion, and (c) multiple trapping and release events involving shallow traps. Pulse dispersion is measured by

numerically differentiating the photocurrent tail and determining the full width half maximum (FWHM) time Δt, as illustrated in Figure 5.13.

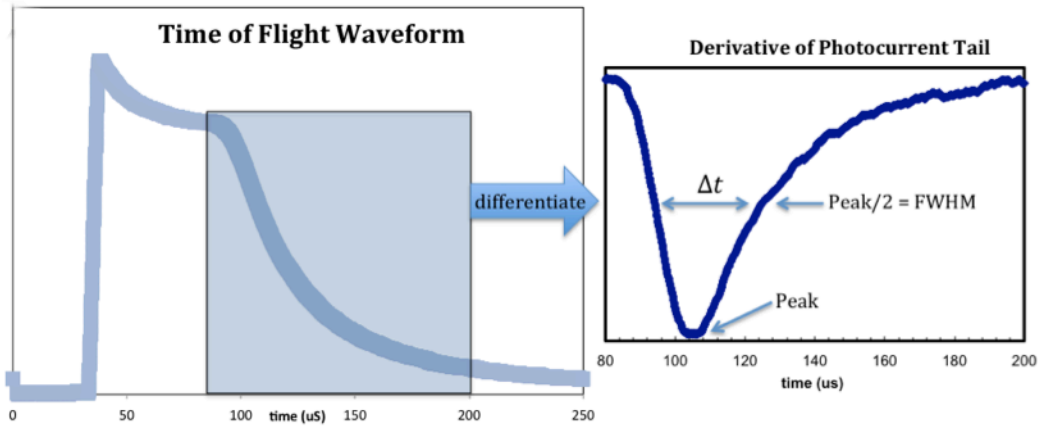

Figure 5.13 To measure pulse dispersion width (Δt) the tail of the photocurrent is numerically differentiated to find the inflection point (peak) and the FWHM value of the pulse dispersion.

5.6.2 Results

Pulse dispersion vs. thickness behavior at 1 V/μm and 4 V/μm is shown in Figure 5.14. Note that Δt is the dispersion of the charge packet in the time domain.

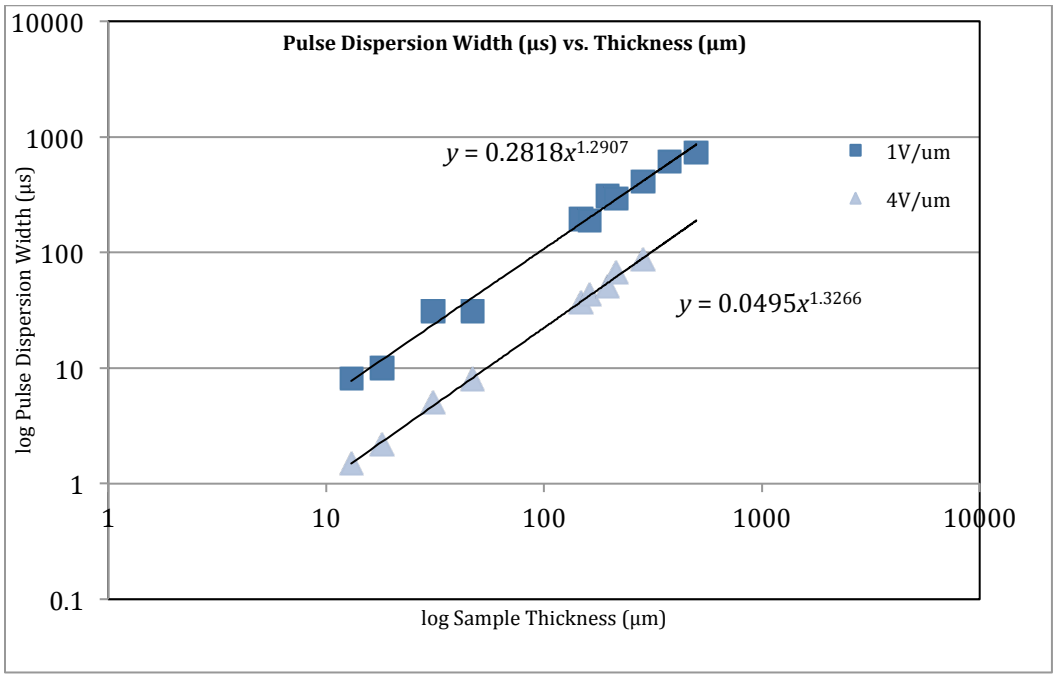

Figure 5.14 Pulse dispersion vs. thickness.

The dispersion in Figure 5.14 shows a power law relationship $\Delta t \sim L^m$ where $m \sim 1.3$. As expected, higher fields lead to lower dispersion, as the carrier transit time is shorter, allowing for less interaction with shallow traps. The modeling of the dispersion as a function of sample thickness would involve the effects of multiple trapping in the presence of the density of states distribution shown in Figure 5.7. Such modeling is beyond the scope if this work. However, it is clear that the dispersion is significant. The measurements shown in Figure 5.14 are all at a given field. The transit time t_T for sample of thickness L under an applied field of F is given by $t_T = L/\mu F$ where μ is the average drift mobility. Consequently, the temporal dispersion Δt depends on the transit time as $t_T{}^m$. Further, if we multiply Δt by the average drift velocity μF, we would get the spatial dispersion Δx of the carrier packet. Thus, approximately $\Delta x \propto t_T{}^m$ or $\Delta x \propto t_T{}^{1.3}$. This result will have to be interpreted in terms of multiple trapping in the presence of the DOS shown in Figure 5.7.

5.7 Summary

Chapter 5 presented the TOF and IFTOF experimental results on the study of the thickness dependence of electron mobility and lifetime for undoped a-Se samples with a thickness in a range of 13 μm to 501 μm. These results show that electron mobility decreased slightly with increasing thickness and that electron lifetime is relatively constant in samples thicker than ~50 μm but drops off sharply in thinner samples.

The combined mobility and lifetime results suggest the existence of a third intermediate trapping level located between the shallow and deep traps described in the discrete binary model of charge transport. Evidence of this intermediate trap level was previously reported by Koughia et al. [46] with the peak concentration occurring around 0.45-0.55 eV below the conduction band. This third trap level has a corresponding release time $\tau_{r3} \sim 3 - 300$ μs which is longer than typical transit

times in thin samples resulting in a drastic decrease in carrier lifetime as the electrons trapped at this level are not released within the timeframe of the experiment. Therefore, this intermediate level can be considered a deep trapping level in thin samples. In thicker samples, with longer transit times, the intermediate trapping level results in a slight decrease in carrier mobility, as mobility is shallow trap controlled.

The effect of the definition of transit time was also described. Three definitions are possible: the inflection point, the half current point, and the knee of the curve. The choice of definition can have a dramatic effect on the calculated mobility and makes the comparison of data difficult without access to the TOF waveforms. The difference in calculated mobility in comparing the inflection point and half current point ranged from ~1% to 24%, where samples with more dispersion showed a much larger difference.

The dispersion of the drifting charge packet causes the tail of the TOF waveform to exhibit an exponential decay to zero as opposed to the ideal TOF waveform where the induced photocurrent immediately drops to zero at t_T. This dispersion is due to: mutual coulombic repulsion between carriers, carrier diffusion, and multiple trapping and release events. Plotting dispersion vs. thickness at two different fields showed a $\Delta t \propto L^m$ type of dependence where L is the sample thickness; and experiments indicate that $m \approx 1.3$. The spatial dispersion Δx of the drifting charge packet distribution at a given field has a dependence on L that follows $\Delta x \propto L^{2.3}$.

6 Summary and Conclusions

6.1 Introduction

The work reported in this thesis specifically studied the thickness dependence of electron transport in pure a-Se photoconductive films. This is a small part of a much larger picture in which flat panel direct conversion X-ray image detectors (such as a-Se based detectors) will become increasingly important in the transition to fully digital radiography. Amorphous selenium has been proven to be a very good photoconductive material for use in flat panel detectors as it meets many of the criteria for an X-ray photoconductor; however much remains unexplained about the actual structure of amorphous selenium. In X-ray photoconductors both electrons and holes must be drifted across the layer and collected. Although hole transport in a-Se has been studied extensively, electron transport remains relatively unexplored, especially its thickness dependence.

6.2 Thickness Dependence of Electron Transport

The thickness dependence of electron transport in a-Se is an important issue both scientifically and technologically, as it places limits on the useful thickness of materials that can be used in detectors. A layer that is too thick may require too high a bias to actually collect the charge carriers, while a layer that is too thin may not absorb a sufficient portion of the incident radiation.

To determine the electron drift mobility, multiple experiments were performed at three different applied (or nominal) fields corresponding to 1, 2, and 4 V/μm for each sample. The TOF waveforms from each experiment were saved and analyzed to determine the electron drift mobility using both the inflection point and half current definitions of transit time.

The measured electron mobility of the eleven a-Se samples manufactured at the University of Saskatchewan for this study ranged from 3.3×10^{-3} cm^2/Vs to 5.21×10^{-3} cm^2/Vs at an applied bias of 2 V/μm. This is well within the expected range of mobility suggested by previous work. The mobility decreased slightly in samples thicker than 50 μm due to the intermediate trap level acting as shallow traps in these samples; shallow traps control drift mobility.

The electron lifetime τ is deep trap controlled and exhibits a sharp drop in thin samples from 524 μs in the 148 μm sample down to 11 μs in the 13 μm sample. This sharp drop can be explained by considering the relationship between the release time from the intermediate trap level and the transit time of the TOF experiment t_T. In thin samples the release time τ_{r3} becomes much longer than t_T at the same electric field (V/μm) causing the electrons trapped at this level to be held for the duration of the experiment, whereas in a thicker sample at the same electric field a longer transit time would allow time for these carriers to be released and once again contribute to the induced photocurrent signal.

The product of the drift mobility and lifetime leads to electron range which, corresponding to the large change in electron lifetime, drops sharply in thinner samples.

6.3 Effect of the Definition of Transit Time

The amorphous structure of a-Se means that deriving a density of states model analytically is difficult. Because of this limitation much of the work to characterize a-Se has been experimental. This experimental investigation requires that parameters such as the transit time t_T be defined. As the TOF technique was being developed the knee of the TOF curve was the only feasible way to measure the transit time, as waveforms could not be saved to a computer for analysis.

The two definitions explored in this work were the inflection point method which defines transit time (t_T) as the time between the inflection points on the leading

edge and tail of the photocurrent signal, and the half current method which defines t_T as the time between the point on the rising and falling edge of the photocurrent where the current is half that of the steady state value. The difference in calculated drift mobility between these techniques ranged from 1% to 24% depending on the length of the photocurrent tail caused by charge packet dispersion. This means that the comparison of drift mobility results must use the same definition of transit time.

6.4 Pulse Dispersion

Pulse dispersion in an X-ray detector will limit device performance by reducing the read out speed. Dispersion of the drifting charge carrier packet in a-Se is greater than can be explained by mutual columbic repulsion and carrier diffusion alone. Multiple trapping and release events in shallow trap levels delay some of the charge carriers as they cross the sample and contribute greatly to the dispersion. The dispersion was measured at two electric fields set to 1 V/μm and 4 V/μm by numerically differentiating the photocurrent tail and defining dispersion Δt as the full width half maximum points on the differentiated curve. Plotting pulse dispersion vs. thickness showed showed a $\Delta t \propto L^m$ type of dependence where L is the sample thickness; and experiments indicate that $m \approx 1.3$. The spatial dispersion Δx of the drifting charge packet distribution at a given field has a dependence on L that approximately follows $\Delta x \propto L^{1.3}$.

6.5 Future Work

To avoid complications due to fractionation from additives such as arsenic used to stabilize a-Se in flat panel detectors pure a-Se was used in this work. Though this simplified the research process, pure a-Se is not suitable for use in a real world detector as it crystalizes much too quickly. Flat panel detectors often use a combination of a-Se with arsenic (As) and a small amount of chlorine added to reduce the negative effects of As on charge transport, typically a-Se:0.2%As + ppm Cl. It would be useful to repeat these measurements using this composition to

confirm the thickness dependence in materials suitable for use in real world detectors. It would also be useful to examine the thickness dependence of hole transport in these materials as both electrons and holes contribute to the final performance of a flat panel X-ray image detector.

7 References

1 Kevles, Bettyann, Holtzmann, "Naked to the Bone Medical Imaging in the Twentieth Century". Camden, NJ. Rutgers University Press, 1996, pp. 19–22.

2 Fogal B., "Electronic Transport Properties of Stabilized Amorphous Selenium X- Ray Photoconductors", M.Sc. Thesis, University of Saskatchewan, Saskatoon, Canada, 2005.

3 Kasap S.O. and Rowlands J.A., "Direct-conversion flat-panel X-ray image sensors for digital radiography", Proceedings of the IEEE, 90, 2002, pp. 591-604.

4 Yaffe M., "Digital mammography", www.sunnybrook.utoronto.ca:8080/~yaffe/ DigitalDetectors.html, Sunnybrook and Women's College Health Sciences Centre, Toronto, 2004.

5 Kasap, S.; Frey, J.B.; Belev, G.; Tousignant, O.; Mani, H.; Greenspan, J.; Laperriere, L.; Bubon, O.; Reznik, A.; DeCrescenzo, G.; et al. Amorphous and polycrystalline photoconductors for direct conversion flat panel X-ray image sensors. Sensors, 11, 2011.

6 Allen, C., "Relaxation in the Electrical Properties of Amorphous Selenium Based Photoconductors", M.Sc. Thesis, University of Saskatchewan, Saskatoon, Canada, 2009.

7 Zhao W. and Rowlands J. A., "X-ray imaging using amorphous selenium: feasibility of a flat panel self-scanned detector for digital radiology", Medical Physics, 22, 1995, pp. 1595-1604.

8 Kasap S.O. and Rowlands J.A., "Review: X-ray photoconductors and stabilized a- Se for direct conversion digital flat-panel X-ray image detectors", Journal of Materials Science: Materials in Electronics, 11, 2000, pp.179-198.

9 Belev G., "Electrical Properties of Amorphous Selenium Based Photoconductive Devices For Application In X-Ray Image Detectors", Ph.D. Thesis, University of Saskatchewan, Saskatoon, Canada, 2007.

10 Que W. and Rowlands J.A., "X-ray photogeneration in amorphous selenium: geminate versus columnar recombination", Physical Review B, 51, 1995, pp. 10500-10507.

11 Kasap S.O. and Rowlands J.A, "Direct-conversion flat-panel X-ray image detectors", IEEE Proceedings: Circuits, Devices, and Systems, 149, 2002, pp. 85- 96.

12 Tanaka K., Maruyama E., Okamoto H., and Shimada T.. "Amorphous Silicon". New York: Wiley, 1999.

13 Mott N.F. and Davis E.A., "Electronic processes in non-crystalline materials", Clarendon Press, Oxford, 1979.

14 Lucovsky G. And Galeener F.L., "Intermediate range order in amorphous solids", Journal of Non-Crystalline Solids, 35-36, 1980, pp. 1209-1214.

15 Kasap S.O., "Handbook of imaging materials", 2nd edition, edited by A. Diamond and D. Weiss, Marcel Dekker, New York, Chapter 9, 2002

16 Adler D. And Yoffa E. J., "Localized electronic states in amorphous semiconductors", Canadian Journal of Chemistry, 55, 1977, pp. 1920-1929.

17 Kastner M., Adler D., Fritzsche H., "Valance-alternation model for localized gap states in lone pair semiconductors", *Physical Review Letters,* **37,** 22**,** pp. 1504-1507,1976

18 Abkowitz M., “On the question of chain-end ESR in amorphous selenium”, Journal of Chemical Physics, 46, 1967, pp. 4537-4538.
19 Agarwal S. C., “Nature of localized states in amorphous semiconductors- a study by electron spin resonance”, Physical Review B, 7, 1973, pp. 685-691.
20 Carles D., Lefrancois G. and Larmagnac J.P., “A model for steady-state photoconductivity in amorphous selenium”, Journal of Physics Letters, 45, 1984, pp. L901-L906.
21 Street R.A., “Hydrogenated amorphous silicon”, Cambridge University Press, London, 1990.
22 Madan A. and Shaw M.P., “The Physics and Applications of Amorphous Semiconductors”, Academic Press Inc., San Diego, 1988.
23 Kasap, S.O., *Optoelectronics and Photonics: Principles and Practices, Second Edition,* Pearson Education, Upper Saddle River, New Jersey, 2011.
24 Mott N.F., “Electrons in disordered structures”, Advances in Physics, 16, 1967, pp. 49-57.
25 Cohen M. H., Fritzsche H. And Ovshinski S. R., “Simple band model for amorphoussemiconductor alloys”, Physical Review Letters, 22, 1969, pp. 1065-1068.
26 Marshall J. M. And Owen A. E., “Drift mobility studies in vitreous arsenic triselenide”, Philosophical Magazine, 24, 1971, pp. 1281-1290.
27 Abkowitz M., “Density of states in a-Se from combined analysis of xerographic potentials and transient transport data”, Philosophical Magazine Letters, 58, 1988, pp. 53-77.
28 Spear W.E., “Transit time measurements of charge carriers in amorphous selenium films”, Proceedings from the Physical Society of London, B70, 1957, pp. 669-675.
29 Orlowski T.E. and Abkowitz M., “Microstripline transient photocurrents in a-Se structure resolved in shallow band tail states”, Solid State Communications, 59, 1986, pp. 665-668.
30 Marini M., Mayer J.W., and Zanio K.R., “Drift velocity and trapping in semiconductors – transient charge technique”, Applied State Science: Advances in Materials and Device Research, edited by R. Wolfe, Academic Press, 1972.
31 Blakney R.M. and Grunwald H.P., “Small-signal current transients in insulators with traps”, Physical Review, 159, 1967, pp. 658-664.
32 Smith W., “Effect of light on Selenium during the passage of an electric current”, Nature, 7, 1873.
33 Hartke J.L. and Regensburger P.J., “Electronic states in vitreous selenium”, Physical Review, 139, 1965, pp. A970-A980.
34 Pai D.M. and Enck R.C., “Onsager mechanism of photogeneration in amorphous selenium”, Physical Review B., 11, 1975, pp. 5163-5174.
35 Polischuk B., “Interrupted Field Time-of-Flight Transient Photoconductivity Technique and its Applications to Amorphous Semiconductors”, Ph. D. Thesis, University of Saskatchewan, Saskatoon, Canada, 1994.
36 Papadakis A. C., “Theory of transient space-charge perturbed currents in insulators”, Journal of Physics and Chemistry of Solids, 28, 1967, pp. 641-647.
37 Hecht K., “Zum mechanismus des lichtelektrischen primärstromes in isolierenden kristallen”, Zeitschrift Fur Physik, 77, 1932, pp. 235-245.
38 Zanio K.R., Akutagawa W.M., and Kikuchi R., “Transient currents in semi- insulating CdTe characteristic of deep traps”, Journal of Applied Physics, 39, 1968, pp. 2818-2828.

39 Akutagawa W. and Zanio K., “The possibility of using CdTe as a gamma spectrometer”, 1968, IEEE Transactions on Nuclear Science, 15, pp. 266-274.
40 Polischuk B., Kasap S.O., and Baillie A., “Study of photogenerated charge carrier dispersion in chlorinated a-Se:0.3%As by the interrupted field time-of-flight technique”, Applied Physics Letters, 63, 1993, pp. 183-185.
41 Kepler R.G., “Charge carrier production and mobility in anthracine crystals”, Physical Review, 119, 1960, pp. 1226-1229.
42 Leblanc O.H., “Hole and electron drift mobilities in anthracine”, Journal of Chemical Physics, 35, 1960, pp. 1275-1280.
43 Brown F.C., “Temperature dependence of electron mobility in AgCl”, Physical Review, 97, 1955, pp. 355-362.
44 Tabak, M.D. and Scharge M., “Transition from emission limited to space charge limited photoconductivity”, 1970, Journal of Applied Physics, 41, pp. 2114-2118.
45 K. Koughia, Z. Shakoor, S.O. Kasap, and J.M. Marshall., “Density of localized electronic states in a-Se from electron time-of-flight photocurrent measurements”, 2005, Journal of Applied Physics, 97.